Computational Studies on Electronic Structure and Optical Properties of a Few Low–dimensional Systems

A Thesis submitted in partial fulfillment
for the degree of

Master of Science

as a part of the
Integrated Ph. D. programme
(Materials Science)
by

S R K Chaitanya Sharma Y

Chemistry and Physics of Materials Unit
Jawaharlal Nehru Centre for Advanced Scientific Research
(A Deemed University)
Bangalore, India.

MARCH 2011

DECLARATION

I hereby declare that the matter embodied in the thesis entitled "**Computational Studies on Electronic Structure and Optical Properties of a Few Low-dimensional Systems**" is the result of investigations carried out by me at the Chemistry and Physics of Materials Unit, Jawaharlal Nehru Centre for Advanced Scientific Research, Bangalore, India under the supervision of Prof. Swapan K. Pati and that it has not been submitted elsewhere for the award of any degree or diploma.

In keeping with the general practice in reporting scientific observations, due acknowledgment has been made whenever the work described is based on the findings of other investigators.

S R K Chaitanya Sharma Y

CERTIFICATE

I hereby certify that the matter embodied in this thesis entitled "**Computational Studies on Electronic Structure and Optical Properties of a Few Low-dimensional Systems**" has been carried out by Mr. S R K Chaitanya Sharma Y at the Chemistry and Physics of Materials Unit, Jawaharlal Nehru Centre for Advanced Scientific Research, Bangalore, India under my supervision and that it has not been submitted elsewhere for the award of any degree or diploma.

Prof. Swapan K. Pati
(Research Supervisor)

Acknowledgements

First of all I would like to thank God Almighty for his transcendent support in this material world and all my Gurus who taught me how to retain my composure in times of anxiety. I owe gratitude to the following people without whose invaluable contribution, this thesis would not be complete.

Firstly, I would like to thank my research supervisor, Prof. Swapan K. Pati for his guidance and support during my research career. His considerable insight and experience in science is inspiring. He has been a source of support in times of difficulty, both in my academic and personal life. In a time of personal tragedy, his words of reassurance gave me much needed relief and comfort. It has been a wonderful experience working with him.

I would also like to thank Dr. Ganga Periyasamy, who is a post-doctoral fellow working jointly with Prof. Swapan K. Pati and Prof. S. Balasubramanian. I am fortunate to have had a chance to work with her on a project. She found time despite of her many commitments to help me in completing a major part of this thesis. I have been fortunate to have a very fruitful collaboration with Prof. C. N. R. Rao, F. R. S and I would like to thank his student Mr. Sandeep Gosh for his assistance in putting together the results. I would like to express my gratitude towards Dr. Ayan Datta. Chapter 4 of this thesis would not have been completed without his effort.

I am very fortunate to have cooperative labmates. They have taught me how to think innovatively and how to make work fun. I would like to thank Arun, Prakash, Ershaad, Ganga, Alex, Dr. Dutta, Dr. Mohakud, Dr. Neihsial, Pralok, Dibya, Wasim Aftab, Wasim Mandal, Pallavi, Dr. Elizabeth, Anisha, Nabanita, Manju, Rukhsan, Sudhakar, Urmit, Oishika, Kriti, Dr. Grisanti and Dr. Sissa. Special thanks go to Arun, Prakash and Ganga who introduced me to the tools that we use in our research and for helping me understand difficult concepts in science. The conversations I had with Ershaad provoked me to look at things from a more human perspective. I appreciate Alex for showing great patience in helping me with various tasks and making things easy for me. I thank Dr. Dutta and Dr. Mohakud for their guidance.

I would like to thank Prof. S. Balasubramanian, coordinator of the Integrated Ph.D programme and who was our first guide at JNCASR. He is the person who always found time to listen to our troubles despite his various more important responsibilities.

I would like to thank all my Integrated Ph.D. course instructors, Prof. S. Balasubramanian, Prof A. Sundaresan, Dr. T. K. Maji, Dr. Govindraj, Prof. Swapan K Pati, Dr. N. S. Vidhyadiraja, Prof. K. S. Narayan, Mrs. Shobha Narayana, Dr. Eswaramoorthy, Prof. Shobhana Narasimhan, Prof. Umesh V. Waghmare, Prof. Amitabh Joshi, Prof. G.U. Kulkarni, Prof. Chandrabhas Narayana, Dr. Ranjan Datta, Prof. S. M. Shivaprasad, Prof. Ranganathan for their excellent courses.

I thank Mr. Nivas, Mrs. Varghese, Mr. A.S. Rao, Mr. Anil, Mr. Vasu, Mrs. Selvi, Mr. Mukthi for their help in my laboratory course work.

My life as an Integrated Ph.D student would have been dull without my batch mates, Arpan, Chidambar, Dileep, Gayatri, Pandu, Rana, Sudeshna and Varun. Thank you Sudeshna for your help during the course work. You made me to understand the difficult concepts in solid state, computational and statistical physics. Chidambar, Arpan and Rana, I remember your help in increasing my knowledge in chemistry. Pandu, Gayatri and Chidambar, I will never forget your great friendship and I can't imagine staying at JNC without your presence. Dileep and Varun, you are the ones who made my life at JNC more memorable. I admire not only your academic excellence but your multiple talents. Thank you for all the help. Dhanya, although you were in Hyderabad during the 2 years of our course work, it was still nice to have you around for the first few days.

I want to thank my friends and everyone who have helped me along my journey. I thank Matte, Sandeep, Kurra, Dasari and Bhadram for their continuous support in both academic and non-academic life and I thank Lowkya, Sivani, Manjusha, Prasoona and Sowjanya for their great friendship. I remember the love of Vijay, Rakesh, Kiran Batta, Leela, Subbu, Sundhar, Saiki, Datta, Praveen, Radha, Yogitha and Tanjua. I thank to my lovely friends Moses, Venkateswarulu, Mallikarjun, Venkatarao, M. H. L. N. Reddy, Gangayya, Santosh, Gopal, Nitesh, Urmi and Manasa. I also thank Satya, Sananda, Sharmila, Pralok, Kanchan, Pramod, Bharath R and Arun R for their help during my course work. I remember my seniors Urmi, Vini, Ritu, Nisha, Nitesh, Abhay, Bivas, Piyush and Sowmik and my juniors Dibya, Darshana, Prasanth and Anindita for their help.

I thank all the academic, administrative, library, complab and hostel staff for providing the facilities in JNC. I especially thank Amit and CCMS staff for their support.

I may have inadvertently missed out some names in this acknowledgement, but that does not diminish my appreciation for them.

Finally, I would like to dedicate this thesis to my parents, my maternal grandparents and my family members for their love and moral support.

Synopsis

Many interesting and counter intuitive properties have been predicted over decades in low-dimensional systems i.e. systems confined to less than three dimensions. In this thesis, we have investigated the electronic structure and optical properties of a few low-dimensional systems viz., graphene, graphene nanoribbons, single-walled carbon nanotubes and chlorophylls.

In chapter 1, we gave a brief introduction to low-dimensional systems and we have mentioned some exotic properties of all the low-dimensional systems which we investigated in this thesis. In this chapter we also introduced the computational and theoretical methods like DFT, TDDFT etc. which we have used to determine the electronic structure and optical properties of the materials.

In chapter 2, we applied density functional theory (DFT) to understand the interaction of halogen/ interhalogen molecules with nanocarbons (graphene and carbon nanotubes). Previous experimental studies on halogen-nanocarbon composites show a charge transfer from nanocarbon to halogens and correspondingly a shift in the Raman G-band of nanocarbons. In our study, we find shifts in the Fermi-level of nanocarbons up on the adsorption of halogen/ interhalogen molecules. Our findings shows that shift in the Fermi-level and the Raman G-band are in accordance with each other and the amount of shift in Fermi-level or Raman G-band depends on the electron affinity character of halogen/ interhalogen molecules.

In chapter 3, we investigated the effect of axial ligation on the structural, redox and absorption properties of a newly discovered chlorophyll, named chl *f*, and explained the reasons for the observed changes. We have also given the reason for the red-shift in the Q_y band of chl *f* compared to other chls, like chl *a* and chl *b*, based on the time dependent density functional theory studies.

Chapter 4 is the final chapter and it is a presentation of work in progress. In this chapter, we studied the structural dependency of the nonlinear optical (NLO) properties of graphene nanoribbons (GNRs). In particular, we considered zigzag GNRs (ZGNRs) of various sizes, both in length and width, and studied the variation in linear and hyper-polarizability by changing the size of ZGNRs. We find that hyper-polarizability value of ZGNRs increases with an increase in the conjugation and the values are large enough to use ZGNRs as donor-acceptor bridges. Calculations of polarizability and hyper-polarizability of ZGNRs attached with different donors and acceptors are in progress.

Contents

List of figures

List of tables

Chapter 1

Introduction

The term, “low dimensional system”, refers to those materials which are finite along at least one dimension. In these systems motion of microscopic degrees of freedom, such as electrons, phonons or photons, is constrained because of their low dimensionality. This constraint to move in three dimensions makes them as hosts for quantum confinement effects. [1-7] Although one would not, traditionally, consider the natural low-dimensional entities such as atoms and molecules as low-dimensional systems, but some of the most exciting recent developments in the field have involved the use of molecules and even biologically important materials, such as DNA, chlorophylls etc. and had blurred the boundaries between the subject and other physical and life sciences. [8] Numerous discoveries in these systems, fascinated researchers for a great part of the last century, and in the last two decades they become one of the primary centers of interest in both condensed matter and materials research.

Mono-layers, thin films, surfaces like graphene are the examples of two-dimensional systems. One-dimensional systems include nanotubes, nanowires and nanorods. Clusters of atoms and quantum dots are examples of zero-dimensional systems. In all these systems there is a reduction in the coordination number at the surface because of the reduction in any one dimension. This creates a high surface to volume ratio which arise new properties that are different from bulk. Many exotic quantum phenomena, such as Aharonov-Bhom effect, persistent currents, phase-coherent transport, quantum Hall-effect and Luttinger liquid [9-21], arise in these systems out of disorder, strong electron-electron interactions and restricted boundary conditions. Low-dimensional systems also admit ordering tendencies which are difficult to realize in three-dimensional materials. Prominent examples are spin- and charge-density waves in quasi-one-dimensional organic compounds and spontaneous circulating currents in two dimensions. [22]

The physics of low-dimensional and bulk systems are often different. A full quantum mechanical treatment of the confined degrees of freedom is required to study these systems. Emergence of experimental techniques such as Scanning tunneling microscopy, Transmission electron microscopy (TEM), molecular beam epitaxial growth of thin-films, chemical vapor deposition, atomic-force microscopy, Ion-beam sputtering, X-ray photoelectron spectroscopy, Auger electron spectroscopy, Electron energy loss spectroscopy, Magnetic force microscopy, High-resolved TEM, High temperature XRD etc. [23-38] provided the path for characterization and fabrication of several novel low-dimensional materials.

In this chapter we will discuss briefly about the low-dimensional materials that we have studied and the computational and theoretical methods which we have used to study these materials. Mainly, we are interested in understanding the electronic and charge transfer properties of these materials. These systems have potential applications in future electronics and our studies give the mechanism of charge transfer and its consequences in these systems. In what follows, we will give a brief overview of graphene, graphene nanoribbons and carbon nanotubes which are two-dimensional, quasi one-dimensional and one-dimensional systems, respectively, in sections 1.1.1 – 1.1.3. In section 1.1.4, we introduce chlorophyll, a zero-dimensional molecule, and we will discuss its importance in photosystems. Section 1.2 gives a brief introduction to nonlinear optics and nonlinear optical properties. Theoretical and computational methods which we used to perform our calculations are mentioned in section 1.3 followed by an outline of the thesis in section 1.4.

1.1 Low Dimensional Systems

1.1.1 Graphene

Apart from the well known allotropes of carbon viz., graphite, amorphous carbon and diamond, scientists have discovered, recently, its other exotic allotropes which include zero-dimensional fullerenes (1985), one-dimensional nanotubes (1991) and very recently graphene (2004), the two dimensional allotrope of carbon. Among the exotic allotropes of carbon, the discovery of graphene was unprecedented in that there were established theoretical concepts precluding its existence. Theoretical argument by Landau and Peirels says that, in low-dimensional crystals, at finite temperatures, thermal fluctuations lead to atomic displacements in the order of inter-atomic distances, and hence, two-dimensional crystals are thermodynamically unstable and could not exist .This argument was latter supported by Mermin and by other experimental observations. [39-43].

Despite of these arguments, there are several attempts to isolate graphene using chemical exfoliation but they resulted in new 3D materials [44] and there are cases in which scientists have grown single and few-layer graphene [45, 46] but their quality and continuity are not known. For the first time, in 2004, physicists from Manchester University extracted high quality graphene crystallites by the micro mechanical cleavage of bulk graphite, for which they were awarded the 2010 Noble prize in physics. [47, 48]

Experimental discovery of graphene didn't violate the above theoretical arguments and is justified by the observation of the ripples in the so-called 2D graphene which affect its properties. [49]. Indeed, it can be argued that, thermal fluctuations and other crystal defects cannot occur in these 2D-crystals because of their small size (<<1 mm) and strong inter-atomic bonds. [40, 43]

Graphene has generated great sensation because of its wondrous properties that may find potential applications. Many groups have been investigating chemically derived graphene as a transparent conductive electrode. [50] For lithium secondary batteries, graphene has shown to be a potential candidate with high lithium storage capacity and this capacity can be further increased by adding other nanocarbons like CNTs and C_{60}. [51] Single-layer graphene is theoretically predicted to have a large surface area of 2600 m^2/g, and experimental findings shows an uptake of 3 wt % for H_2 at 100 bar and 300 K and 35 wt % for CO_2 at 1 atm and 195 K for few-layer graphene. [52] Magnetic properties of graphene shows that dominant ferromagnetic interactions coexist along with anti-ferromagnetic interactions somewhat similar to frustrated systems. Elastic modulus and hardness of polyvinyl alchol and poly (methyl methacrylate) composites have been shown to increase significantly when they are reinforced with small quantities of few-layer graphene. [53]

Finally, exotic electronic properties of graphene, reflects its structural flexibility. [54] Single layer graphene is a 2D zero-gap semiconductor with a linear dispersion relation near the K-point of the Brillouin zone resembling the Dirac spectrum for massless ferimons. [55, 56] This linear dispersion relation can be easily derived using the tight binding approximation including the nearest neighbors. [57] Graphene also acts as a platform to observe several exotic phenomena, like, ballistic electron transport, anomalous integer quantum Hall effect at room temperatures and fractional quantum Hall effect at low temperatures [58], Klein-paradox [59] etc. Electronic and magnetic properties of graphene can be tuned by doping or molecular interactions. Changes in these properties due to molecular charge transfer can be observed clearly using Raman spectroscopy and should be explored for applications.

1.1.2 Graphene Nanoribbons (GNRs)

These are the quasi-one-dimensional materials obtained by the finite termination of graphene along one direction, the other direction being infinite. Depending on their edge geometry GNRs are divided into two classes, namely, zigzag GNRs (ZGNRs) and Armchair GNRs (AGNRs). Because of their contrasting boundary conditions, which arise because of their different edge geometries, these nanoribbons show different electronic structure properties. These systems can be prepared experimentally either through "top-down approach", which includes techniques like etching graphene with a STM tip, Lithographic patterning on epitaxially grown graphene, unzipping and unrolling of carbon nanotubes by epoxidation of CNTs etc., or through "bottom-up approach", which includes combining small organic molecules to build giant carbon structures using elegant synthetic methods.

Among these GNRs, ZGNRs exhibit interesting electronic properties due to the presence of localized electronic states, known as edge states, which are absent in the case of AGNRs. Edge states allow fine tuning of the electronic structure and band gap of ZGNRs through structural or chemical modifications along with doping and external perturbations. Metal free magnetism can be achieved using semiconducting ZGNRs as they show semi-metallic behavior under external perturbations [60]. By selective doping ZGNRs can be tuned to use as spin filters and spin transistors. [61-63]

Because of their finite width along one direction, optical response of GNRs is anisotropic for transversely polarized and longitudinally polarized photons. Transverse and longitudinal polarized components are energetically well separated in the case of AGNRs and are mixed for the case of ZGNRs. [64] There are few studies on the nonlinear optical properties of GNRs and recent experimental reports shows that because of their integrated crystalline structure and electronic conjugation, GNRs exhibit stronger third-order nonlinearities and optical limiting responses compared to the graphene oxide nanoribbons. In addition, ZGNRs are predicted to possess open-shell singlet ground states with diradical characteristics. [65-67] Considering these facts we investigated the first hyper-polarizability of ZGNRs of various widths in chapter 4.

1.1.3 Carbon Nanotubes

These are the one-dimensional allotropes of carbon and can be visualized as a graphene sheet rolled into a cylinder. Their discovery marks a major event in the area of carbon materials and more so in one dimensional materials. CNTs are characterized by a pair of chiral indices (n, m), with n and m being two integers, which specify the CNT uniquely. [68] The integers n and m denote the number of unit vectors along two directions in the honeycomb crystal lattice of graphene. Nanotubes are called zigzag if m=0 and are called armchair if n=m. Otherwise, they are called chiral. Their electronic structure is either metallic or semi-conducting depending on (n, m). [51]

Multi-walled carbon nanotubes (MWNTs) were first prepared by arc discharge of graphite [69] and several alternative methods of synthesis were also reported later. [70, 71] The properties of Single walled carbon nanotubes (SWNTs) are of special interest for applications, since these materials possess interesting electronic band structure. Electronic band structure of SWNTs can be derived easily from a graphene sheet while neglecting hybridization effects due to the finite curvature of the tube structure. Because of its electronic structure, CNTs acts as ideal test beds for studies of quantum confinement effects like ballistic conductance [72], Kondo effect and spin-injection [73, 74], Luttinger liquid behavior [75], and single and double quantum dot states. [76]

SWNTs and polyvinyl alcohol composite fibers show toughness unmatched in the man-made and natural worlds. [77] Semiconducting SWNTs have a channel conductance that can be modified by orders of magnitude ($\sim 10^5$) by an externally applied gate voltage, very similar to that of a MOSFET. [78] Dispersion of carbon nanotubes in synthetic graphite (ca. 3 wt %) give rise to a continuous conductive network as well as a mechanically strong electrode, resulting in a doubled energy efficiency of lithium-ion-batteries. [79] SWNTs have been employed in gas-sensors and have advantages over conventional metal-oxide-based sensors in terms of power consumption, sensitivity, miniaturization, and reliable mass production. [80] Electronic and molecular properties of CNTs can also be tuned by doping or through molecular charge transfer, similar to graphene. Once again, Raman spectroscopy can be used as a probe to understand the changes due to charge transfer. Interaction of SWNTs with electron withdrawing and electron donating molecules shows stiffening and softening in the G-band of Raman spectra, respectively. [81] Effect of charge transfer due to halogen molecules on CNTs and graphene are explored in chapter 2 of this thesis.

1.1.4 Chlorophylls

Chlorophyll is an essential and abundant pigment present in the plants, algae and cyanobacteria. [82] Chlorophyll is vital for photosynthesis, a process in which solar energy is converted into chemical energy. Chlorophyll molecules are presented in and around photosystems which in turn present in the thylakoid membranes of chloroplasts (see figure 1).

Chloroplasts are organelles found in plant cells and other eukaryotic organisms. It consists of a material called as “stroma”. The sub-organelles, thylakoids, are presented as stacks within the stroma. [83] Empty area inside the thylakoid is called as thylakoid space or “lumen”. The membrane separating the stroma from lumen is called as thylakoid membrane and photosynthesis takes place on this membrane. Light harvesting complexes (LHC) also present in thylakoid membranes and each LHC consists of light-absorbing pigments, including chlorophylls, carotenoids and proteins, which funnel the incident solar energy to reaction centre through resonance energy transfer. In photosystem II (PSII) of higher plants, a special pair of chlorophylls, named as P680, (here P denotes pair of chlorophylls and the number 680 denotes the absorption maximum of that pair), present at the reaction centre and receives the funneled energy and utilizes it for charge separation and charge transfer followed by several other processes to finally reduce the absorbed CO_2 from atmosphere to sugars. Thus, chlorophyll functions in photosystems both as a light harvesting pigment in LHC and as a charge separator at RC.

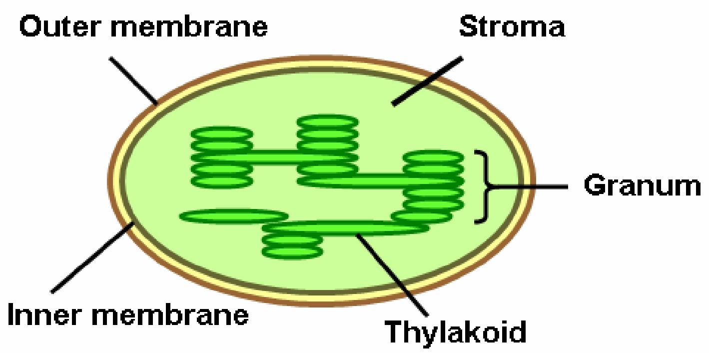

Figure 1.1 Thylakoid (green) inside a chloroplast (source: Wikipedia [84])

Structure of chlorophyll mainly consists of a substituted chlorin ring with Mg atom at the centre of the ring and a phytol chain (see figure 1.2). Chlorin ring is a reduced porphyrin ring, which consists of four pyrrole units connected to each other through methane bridges (see figure 1.3). If the porphyrin ring is doubly reduced then it is called as Bacteriochlorin ring. A chlorophyll molecule without an Mg atom at its centre is called as pheophytin.

At present there are 5 kinds of chlorophylls known, which can perform oxygenic photosynthesis, viz. chl a, chl b, chl c, chl d and chl f. Chlorophylls are generally penta-coordinated in nature [85] and there is a strong effect of this 5th coordination on the structure of chlorophyll. Major structural changes include Mg-N bond distances and out of plane distance of Mg i.e. distance of Mg from the plane of the chlorin ring. Penta-coordination also affects the redox potential of the chlorophyll molecule. Across the electron transport chain in PSI this 5th coordination to chlorophylls is arranged in such a manner to maintain a forward electron transfer. [85]

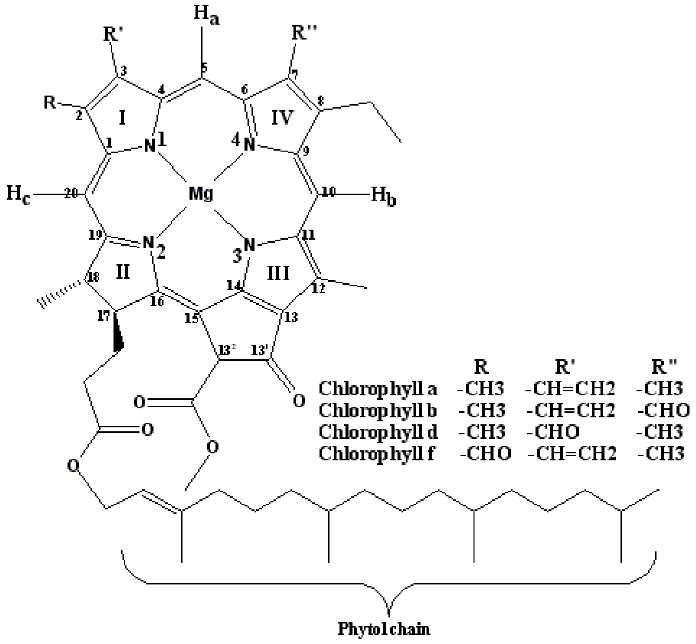

	R	R'	R''
Chlorophyll a	-CH3	-CH=CH2	-CH3
Chlorophyll b	-CH3	-CH=CH2	-CHO
Chlorophyll d	-CH3	-CHO	-CH3
Chlorophyll f	-CHO	-CH=CH2	-CH3

Figure 1.2 Schematic representation of chlorophyll

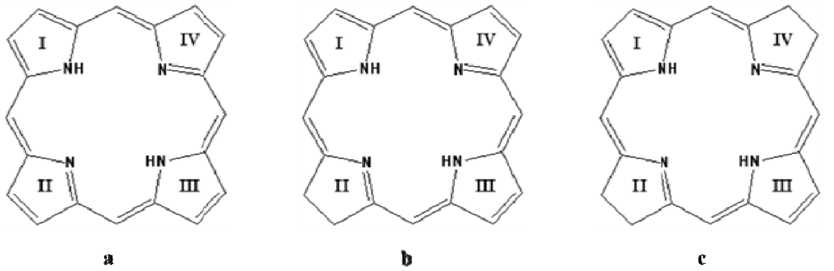

a b c

Figure 1.3 Schematic representation of a) Porphyrin (D_{4h}) b) chlorin (C_{2v}) c) Bacteriochlorin (D_{2h})

Chlorophylls with different absorption maximum, due to their different environment, are arranged in an energy hierarchy to transfer the light to the reaction centre, as mentioned earlier. Absorption spectrum of chlorophyll is very sensitive to the changes occurring on the chlorin ring. [86] A typical absorption spectrum of chlorophyll consists of high energy B (Soret) – bands and low energy Q-bands. Goutermann has proposed his four-orbital model to explain the absorption spectra of porphyrins, substituted porphyrins and its derivatives (chlorin and bacteriochlorin) [87, 88]. According to this rule, the absorption bands in porphyrin systems arises from the transition between the $a_{1u} \rightarrow e_g$ and $a_{2u} \rightarrow e_g$ (here HOMO, HOMO – 1 orbitals possess a_{1u}, a_{2u} symmetry respectively and both the orbitals LUMO and LUMO + 1 possess e_g symmetry). Relative energies of these transitions are affected by the substituents on the ring and the metals present at the centre of the ring. It should be emphasized that, four-orbital description is generally accurate for Q-bands but not for B-bands.

In porphyrin, HOMOs with a_{1u} and a_{2u} symmetry are nearly degenerate and LUMOs with e_g symmetry are degenerate. Excitations between these four orbitals will lead to two transitions of y-symmetry (i.e., transition dipole moment in the 'y'–direction) and two transitions of x-symmetry. (i.e., transition dipole moment in the 'x'–direction). The two lower transitions among these four are termed as Q-bands (Q_y and Q_x) and the upper transitions are termed as B-bands (B_y and B_x). A transition dipole moment which passes through the two opposite pyrrole rings along the y-axis of the porphyrin characterizes a Q_y band. [86] In the case of porphyrin, as both the transitions, $a_{1u} \rightarrow e_g$ and $a_{2u} \rightarrow e_g$ of ^1E_u character are nearly degenerate, mixing of these transitions leads to a lower intense Q-band and a higher intense Soret-band. [46]

In the case of chlorin, reduction in symmetry lifts the degeneracy of the LUMOs which causes a decrement in the mixing of excitations. As excitations are not mixed much, intensities of both the Q and B-bands remain high. Once there are substitutions on the chlorin ring symmetry of the ring will be completely destroyed and this leads to an increment in the intensity of Q-band. Increase in the intensity of Q-band reflects the fact that, there is a greater absorption probability and this helps for efficient energy transfer between the component chromophores, which is important for photosynthetic systems. [86]

In this thesis, we studied newly discovered chlorophyll, named as, chlorophyll *f*. Chl *f* can perform oxygenic photosynthesis and its Q_y absorption maximum in the infrared region. This shows that, in low light conditions also chl *f* can perform oxygenic photosynthesis. As mentioned by Prof. James Barber, this ability of chl *f* can be used for the design of photovoltaic cells. [89] This is because, over half of the light from the sun comes in at infrared wavelengths and the makers of photovoltaic panels have been working on ways to extend the section of the spectrum that solar cells can absorb to beyond red. By the discovery of chl *f*, now, we can absorb the infrared region of solar spectrum by chl *f*. Chl *f* can also be used for the artificial photosynthesis technology. [89] Considering these facts, we studied the effects of axial ligation and the cause for the red-shift in the Q_y absorption maximum of chl *f*.

1.2 Nonlinear Optics

When a material is exposed to an external electric field, it becomes polarized with an induced dipolemoment. If the incident field is weak one can write polarization as

$$P = \chi E \qquad (1.2.1)$$

where, χ is called the polarizability of the medium. At molecular regime, this external electric field distorts the electron distribution in the molecule which leads to the molecular polarization (μ) given by

$$\mu = \alpha E \qquad (1.2.2),$$

where, α is the polarizability of the atom or molecule and is directly proportional to the number of charges present in the system. Thus, for atoms or molecules the polarizability increases with their size. If the incident field is strong then equation 1.2.1 changes to

$$P = \chi^{(1)} E + \chi^{(2)} EE + \chi^{(3)} EEE + \ldots \qquad (1.2.3),$$

where, $\chi^{(n)}$ is the nth – order susceptibility of the medium and is a tensor of rank (n+1) . [90] Thus, the optical characteristics of a material, such as refractive-index, dielectric-permittivity etc. which depend on the susceptibility, become as a function of the electric field if the incident electric field is strong, i.e. they are no more linear with the applied electric field. This nonlinear optical (NLO) behavior can be clearly seen by substituting a sinusoidal field

$$E = E_0 + E_1 (\cos \omega t) \qquad (1.2.4),$$

ω being the frequency of the incident electric field, in the equation (1.2.3). Substituting 1.2.4 in 1.2.3 gives

$$P = [E_0 + E_1 (\cos \omega t)]\, \chi^{(1)} + [E_0 + E_1 (\cos \omega t)]^2\, \chi^{(2)} + [E_0 + E_1 (\cos \omega t)]^3\, \chi^{(3)} + \ldots \qquad (1.2.5).$$

Using trigonometric identities and rearranging the terms in 1.2.5 one obtains,

$$P = [E_0 + E_1 (\cos \omega t)]\, \chi^{(1)} + [E_0^2 + (1/2)\, E_1^2 + 2\, E_0\, E_1(\cos \omega t) + (1/2)\, E_1^2 (\cos 2\omega t)]\, \chi^{(2)} + [E_0^3 + (3/2)\, E_0E_1^2\, (1 + \cos 2\omega t) + 3E_0^2E_1\, (\cos \omega t) + (3/4)\, E_1^3 (\cos \omega t + \cos 3\omega t)]\, \chi^{(3)} \ldots \qquad (1.2.6).$$

In the above equation, the processes associated with $\chi^{(2)}$ are called second-order optical processes and the processes associated with $\chi^{(3)}$ are called third-order optical processes. Observation of second-order optical processes are restricted to non-centrosymmetric medium, whereas, the third-order optical processes can take place in any random or ordered medium.

NLO phenomena includes light mediated processes like second harmonic generation (SHG), optical-Pockels effect, optical-Kerr effect, two-photon absorption (TPA) etc. [90, 91] For a material to exhibit interesting NLO properties both the individual molecular hyper-polarizability (β or γ) and the orientation effects have to be optimized. In general, charge distribution due to π-electrons is easily deformable and hence, they give rise to large molecular hyper-polarizabilities. In this thesis, we mainly consider those NLO properties of graphene nanoribbons (GNRs) which are mostly governed by the polarizations of the electronic states i.e. applied electric field will not affect the lattice structure. To be clear, we will calculate the linear polarizability (α) and the second hyper-polarizability (γ) of GNRs of varying length and width. Methods which we followed to calculate γ and its relation with $\chi^{(3)}$ are given in chapter 4.

1.3 Theoretical and Computational methods

1.3.1 Density Funcional Theory:

Methods based on many-electron wave functions are often found to be very computationally expensive and difficult for many-electron systems. An alternative to the many-electron wave function based methods is density functional theory (DFT) which is essentially derived from the Thomas-Fermi-Dirac equations. [92] The rigorous foundation of DFT is based on the two Hohenberg-Kohn theorems.

- **The Hohenberg and Kohn existence theorem:** This states that the ground state energy and all other ground state molecular properties are uniquely determined by the ground state electron density. That is, the energy of an electronic system can be expressed in terms of the electron probability density $\rho(\mathbf{r})$ which represents the total electron density at a particular point in space r. The electronic energy $E[\rho(\mathbf{r})]$ is said to be a functional of the electron density. Thus, for every given density there is a specific energy.

- **The Hohenberg-Kohn variational theorem:** This theorem introduces the variational principle into the DFT. It states that the ground state energy can be obtained variationally and the density which minimizes the total energy is the exact ground state density. In other words, for every trial electron density $\rho(r)$, the computed $E[\rho(\mathbf{r})]$ is greater than or equal to exact ground state energy $E[\rho_o(\mathbf{r})]$.

1.3.2 Kohn-Sham Self-Consistent Field Methodology:

The Hohenberg-Kohn theorem does not tell us how to calculate the ground state electron density without reference to the wave function. Kohn and Sham (1965) realized that the Hamiltonian operator could be constructed for a system of non-interacting electrons in an effective potential. Eigenfunctions of this Hamiltonian are the Slater determinants of the one-electron eigenfunctions and such a Hamiltonian can be expressed as a sum of one-electron operators. [92] The eigenvalues are simply the sum of the one-electron eigen values. Kohn-Sham considered a fictitious system of non-interacting electrons that have for their overall ground-state density the same density as some real system of interest where the electrons do interact. The energy functional is divided into specific components to facilitate further analysis,

$$E[\rho(r)] = T_{ni}[\rho(r)] + V_{ne}[\rho(r)] + V_{ee}[\rho(r)] + \Delta T[\rho(r)] + \Delta V_{ee}[\rho(r)] \tag{1.3.1}$$

where, the terms on the right hand side refer to the kinetic energy of the non-interacting electrons (T_{ni}), the nuclear-electron interaction (V_{ne}), the classical electron-electron repulsion (V_{ee}), the correction to the kinetic energy deriving from the interacting nature of the electrons (ΔT), and all non-classical corrections to the electron-electron repulsion energy (V_{ee}).

For a system of non-interacting electrons the kinetic energy is just the sum of the individual electron kinetic energies. The difficult term in the above equation is ΔT and ΔV_{ee} and have been added together to give E_{xc}, the exchange correlation energy. This includes not only exchange and correlation energy but also the correction for the classical self-interaction energy and the difference in kinetic energy between the fictitious non-interacting system and the real one.

The Kohn-Sham orbital were determined by the same procedure as in the MO theory, determining the individual orbital coefficients by solution of the secular equation and following the same procedure as in HF theory except that the elements $F_{\mu\nu}$ are replaced by F^{KS} defined as,

$$F^{KS} = \left\langle \chi_\mu \left| -\frac{1}{2}\nabla^2 - \sum_{ki} \frac{Z_k}{R_i} + \int \frac{\rho(r)}{|r-R|} dr + V_{xc} \right| \chi_v \right\rangle \tag{1.3.2}$$

where, V_{xc} is the functional derivative, $\delta E_{xc}/\delta\rho$. All the terms can be evaluated from the electron density (ρ), except the term $E_{xc,}$ whose functional form is unknown. Fortunately, for systems in which electrons are not highly correlated, E_{xc} is relatively small. The key to accurate KS DFT calculation of molecular properties is to get a good approximation of E_{xc}.

Several different schemes have been developed for obtaining approximate form for the functional for the exchange-correlation energy. The main source of error in DFT usually arises from the approximate nature of $E_{xc.}$ E_{xc} is expressed in terms of electron density as the interaction between the electron density and an energy density φ_{xc} that is dependent on the electron density,

$$E_{xc}[\rho(r)] = \int \rho(r)\varphi_{xc}[\rho(r)]dr \tag{1.3.3}$$

In LDA, the energy density φ_{xc} is treated as a sum of individual exchange and correlation energy per electron in a homogenous electron gas with the electron density (ρ).[92, 93]

$$\varphi_{xc}(\rho) = \varphi_x(\rho) + \varphi_c(\rho) \tag{1.3.4}$$

where,

$$\varphi_x(\rho) = -\frac{3}{4}\left(\frac{3}{\pi}\right)^{1/3}(\rho(r))^{1/3} \tag{1.3.5}$$

The term Local Density Approximation (LDA) has been used to indicate any density functional theory where the value of φ_{xc} at the position of **r** could be computed from the value of ρ at that position. The functionals that conform to this definition are those derived from the uniform electron gas where the density has the same value at every position. The correlation part φ_c (ρ) was calculated by Vosko, Wilk and Nusair (VWN) using the VWN formalism. [92] However, in molecular systems the electron density is far from spatially uniform and the way to improve the correlation functional is to make it depend not only on the local value of the density but also on the extent to which the density is locally changing i.e., the gradient of the density. This is called gradient corrected or generalized gradient approximations (GGA). Using the GGA, very good results for molecular geometries and ground-state energies have been achieved.

Potentially more accurate than the GGA functionals are the meta-GGA functionals. These functionals include a further term in the expansion, which depends on the density, the gradient of the density and the Laplacian of the density. Difficulties in expressing the exchange part of the energy can be relieved by including a component of the exact exchange energy calculated from Hartree-Fock theory. Functionals of this type are known as hybrid exchange correlation functional. A hybrid exchange-correlation functional is usually constructed as a linear combination of the Hartree-Fock exact exchange functional and any number of exchange and correlation explicit density functionals. The parameters determining the weight of each individual functional are typically specified by fitting the functional's predictions to experimental or accurately calculated thermo-chemical data. For example, the popular B3LYP functional can be written as, [85]

$$E_{xc}^{\mathrm{B3LYP}} = E_{xc}^{\mathrm{LDA}} + a_0(E_x^{\mathrm{HF}} - E_x^{\mathrm{LDA}}) + a_x(E_x^{\mathrm{GGA}} - E_x^{\mathrm{LDA}}) + a_c(E_c^{\mathrm{GGA}} - E_c^{\mathrm{LDA}}) \tag{1.3.6}$$

where, a_o= 0.20 ,a_x = 0.72 and a_c = 0.81 are the three empirical parameters determined by fitting the predicted values to a set of atomization energies, ionization potentials, proton affinities, and total atomic energies.

1.3.3 Time-dependent Density Functional Theory:

Time-dependent density-functional theory (TDDFT) extends the basic ideas of ground-state density-functional theory (DFT) to the treatment of excitations or more general time-dependent phenomena. [85, 93] TDDFT can be viewed an alternative formulation of time-dependent quantum mechanics, but, in contrast to the normal approach that relies on wave-functions and on the many-body Schrodinger equation, its basic variable is the time-dependent electron density, n(**r**, t). The advantages are clear: The many-body wave-function, a function in a 3N-dimensional space (where N is the number of electrons in the system), is a very complex mathematical object, while the density is a simple function that depends solely on 3 variables, x, y and z. The standard way to obtain n(**r**, t) is with the help of a fictitious system of non-interacting electrons, the Kohn-Sham system. The final equations are simple to tackle numerically, and are routinely solved for systems with a large number of atoms. These electrons feel an effective potential, the time-dependent Kohn-Sham potential. In the time-dependent case, these Kohn-Sham electrons obey the time-dependent Schrodinger equation

$$i\frac{\partial}{\partial t}\varphi_i(r,t) = \left[-\frac{\nabla^2}{2} + v_{KS}(r,t)\right]\varphi_i(r,t)$$

(1.3.7)

The density of the interacting system can be obtained from the time-dependent Kohn-Sham orbitals

$$n(r,t) = \sum_i^{occ} |\varphi_i(r,t)|^2$$

(1.3.8)

1.3.4 Nuclear Magnetic Resonance (NMR) Spectroscopy:

Nuclear Magnetic Resonance (NMR) spectroscopy is probably the most widely applied spectroscopic technique in modern chemical research. The molecular properties responsible for the generation of NMR spectra i.e., the nuclear magnetic shielding constants and indirect nuclear spin-spin coupling constants were identified and analyzed in terms of perturbation theory over 40 years ago by Ramsey. [94] However because of the practical problems associated with the calculation of these properties, the early applications of *ab initio* methods to the study of NMR parameters were not particularly successful. In recent years, these obstacles have been partly-overcome as a result of a general improvement in *ab initio* techniques and computer technology, and partly through the development of special methods and programs for the calculation of NMR properties. As a result, over the last 5-10 years, the calculation of NMR parameters by *ab initio* methods have developed into a useful and popular tool of computational quantum chemistry. **[85, 92]**

1.3.4.1 Chemical shift:

The magnetic field at the nucleus is not equal to the applied magnetic field; electrons around the nucleus shield it from the applied field. The difference between the applied magnetic field and the field at the nucleus is termed the nuclear shielding. When we place a nucleus with surrounding electron clouds in an external magnetic field, it induces its own field in a direction opposite to the applied field. The net field experienced by that nucleus is,

$$\gamma_{eff} = \gamma_0 - \gamma_i$$

(1.3.9)

where, γ_0 is the field experienced by the bare nucleus, γ_i is the field experienced by the shielded nucleus.

$$\gamma_i = \sigma_i^* \gamma_0$$

(1.3.10)

Using (1.3.10) in (1.3.9) and rearranging

$$\sigma_i = \gamma_0 - \frac{\gamma_i}{\gamma_0}$$

(1.3.11)

where, σ_i = the absolute magnetic shielding of any nucleus.

Thus, absolute chemical shielding or nuclear magnetic shielding is the difference between the frequency (field experienced) of the bare nucleus, γ_0, and the frequency of the same nucleus in the species under investigation, γ_i. This nuclear magnetic shielding constant σ_i is a molecular electronic property and is independent of the field. Experimentalists are unable to measure magnetic shielding (σ) due to their inability to know the magnitude of magnetic field to accuracy of the order of parts per billion (ppb). So a relative quantity- "Chemical Shift" (δ), which relates the shielding of the species (σ) under investigation and the shielding of the same nucleus in a reference compound (σ_{ref}) is being used.

1.3.4.2 NMR SHIELDING (σ_i) and DFT:

Density Functional-based calculations of magnetic properties, especially of NMR chemical shifts, provide excellent results for lighter elements. [85, 92] In these calculations the wave function can be expressed as static second derivatives of the total energy with respect to the two perturbations. Thus two derivatives with respect to magnetic field and nuclear magnetic moment give the NMR shielding.

$$\sigma_{ji}^N(ppm) = \frac{\partial^2 E}{\partial B_i \partial M_{Nj}}$$

(1.3.12)

where, i and j are the components of the external magnetic field and induced magnetic moment, respectively. From the Kohn-Sham derivation (1.3.3), the exchange functional is

$$E_{xc}[\rho(r)] = \int \rho(r)\varphi_{xc}[\rho(r)]dr$$

(1.3.13)

Now we introduce the magnetic field $\vec{\mathbf{B}}$, by means of the so-called minimal coupling.

$$\vec{P} \overset{substitute}{\longrightarrow} \vec{P} + \frac{\vec{A}}{c}$$

(1.3.14)

where, $\vec{\mathbf{A}}$ is the vector potential of the field ($\vec{\mathbf{B}}$) and $\vec{\mathbf{P}}$ is the momentum operator. Now exchange energy, E_{xc}, becomes a functional of the relativistic four current density, which translates in non-relativistic to the electron density ρ and the ring current density $\vec{\mathbf{j}}$,

$$E_{xc}(\rho) \overset{substitute}{\longrightarrow} E_{xc}[\rho, \vec{j}]$$

(1.3.15)

The current density J is expressed as an orbital dependent quantity.

$$J(\vec{r}) = \sum n_k \left[\underset{\textbf{I}}{\frac{i}{2}(\psi_k \vec{\nabla}\psi_k^* - \psi_k^* \vec{\nabla}\psi_k)} - \underset{\textbf{II}}{\frac{i}{c}\vec{A}\psi_k\psi_k^*} \right]$$

(1.3.16)

where, n_k denotes the occupation number, k is the orbital index, $\vec{\mathrm{A}}$ is the vector potential, c is the speed of light, and ψ_k is the molecular orbital. Term (II) of the sum is zero if no magnetic field is applied. In the presence of a magnetic field, this term is called the diamagnetic contribution, and term (I) describes the paramagnetic contribution of current density. The total current density J is a sum over contributions of all occupied orbitals $j_{k.}$ Each contribution j_k is directly related to a molecular orbital ψ_k. The difficulty in the DFT method is the gauge problem (for any given magnetic field, there is considerable freedom in the choice of gauge for vector potential, in particular vector potential depends on the (arbitrary) coordinate origin. It is called gauge problem). The numerical methods have been developed as remedy for the gauge problem in DFT. The best solution to the gauge problem is to employ the Gauge Including Atomic Orbital (GIAO) as basis functions.

1.3.4.3 GIAO method:

An elegant way of dealing with the gauge problem is through the use of explicitly field dependent basis functions. [85]It was first proposed by London in 1937. The GIAO method for calculating magnetic properties uses the following explicit field-dependent basis set functions.

$$\chi_\mu(\vec{B}) = \exp\left[-\frac{i}{2c}(\vec{B} \times \vec{R_\mu})^\times r\right] \chi_\mu(\vec{O}) \tag{1.3.17}$$

where, R_μ is the position vector of basis function χ_μ and $\chi_\mu(\vec{O})$ denotes the usual field-independent basis function.

The GIAO is thus a gauge transformed atomic orbital, with the new gauge origin at the nucleus. The GIAOs are better viewed as gauge transformation of the individual basis functions. Since the atomic orbitals are inherently local, such transformation has only a local field effect, thereby ensuring an optimal gauge for the atomic orbital. The use of GIAOs eliminates any explicit reference to the global gauge origin. GIAOs are not proper gauge transformations neither of the wave function, nor of the molecular orbital and their use does not make the energy gauge invariant. GIAOs do, however, ensure rapid basis set convergence for many second order magnetic properties, and thus resolve the gauge problem.

1.4 Outline of the thesis

This thesis consists of 4 chapters. In chapter 2, we studied the changes in the electronic structure of graphene and carbon nanotubes up on their interaction with halogen/ interhalogen molecules. Our study gives an insight for the cause for changes observed in the Fermi-level shift. In chapter 3, reason for the red-shift in the Q_y band of chl f compared to its structural isomer chl *b* is given. Effects of fifth coordination on structural, redox and absorption properties of chl *f* are studied using several axial ligands which are highly available in nature as fifth coordination. Finally, in chapter 4 we studied the changes in polarizability and hyper-polarizability of ZGNRs with a change in their length and width. Our results show that these ZGNRs can be used as donor-acceptor bridges to get materials with high NLO activity.

Chapter 2

Interaction of Halogen Molecules with SWNTs and Graphene

2.1 Introduction

Nanomaterials based on carbon such as single walled carbon nanotubes (SWNTs) and graphene have emerged as exciting materials owing to their interesting properties, the most important ones being related to their electronic structure.[58, 95] These properties of SWNTs and graphene can lead to many potential applications,[96, 97] specially in electronic devices.[98, 99] The ability to tune the Fermi level in these materials by selectively filling (depleting) electrons to the conduction (valence) band therefore becomes relevant, if device applications are to become a reality. Molecular and electrochemical doping provide possible methods of tuning the electronic structure of SWNTs and graphene[100] and the doping level is readily probed by Raman spectroscopy which is useful to examine changes in electronic structure because of the strong electron-phonon correlation in these materials.[100-103] Raman spectroscopy is also a non-invasive technique and can be used in conjunction with other experimental methods. The changes in the electronic band structure of SWNTs and graphene can also be monitored by employing electronic absorption spectroscopy which gives useful, statistically averaged data.[104, 105] Such changes can be understood microscopically through theoretical calculations.

Doping SWNTs is amphoteric as can be seen from the various reports in the literature on the interaction of SWNTs with various electron donor and acceptor molecules [51, 81, 106, 107]. SWNTs can exchange electrons from the dopants irrespective of whether they are electron donating or withdrawing in nature. Thus, an electron-donating molecule such as tetrathiafulvalene (TTF) causes changes in the spectroscopic signatures opposite to those due to an electron-withdrawing molecule such as tetracyanoethylene (TCNE).[81] The S_{22} band in the electronic absorption spectrum of SWNTs[81] shifts to higher energy on interaction with TCNE compared to that of undoped SWNTs while the shift is in the opposite direction in the case of TTF (i.e. S_{22} band shifts to lower energy). The Raman spectrum of SWNTs is markedly affected on interaction with these molecules. Coulombic charge-transfer from metals like gold and platinum to SWNTs also induces significant changes in the Raman spectra of the SWNTs, especially the G-band (~1567 cm $^{-1}$), indicating that the shift in Raman frequency is associated with the shifts in the Fermi level of SWNTs.[81] Similar charge-transfer has been found to occur in the case of metal nanocluster decorated graphene.[108] Studies on the interaction of electron donor and acceptor molecules with graphene have demonstrated similar changes in the Raman spectrum of graphene wherein electron donor molecules such as aniline and TTF shows softening of the G-band.[81] Nitrobenzene and TCNE, on the other hand, stiffen the G-band,[81] a behaviour similar to that of SWNTs. These experimental observations on molecular doping of graphene and SWNT have been corroborated by theoretical studies.[109, 110]

Halogens such as I_2 have traditionally been used as electron withdrawing species to examine their interaction with aromatic molecules.[111-113] It was, hence, of interest to study the interaction of different halogen molecules with extended π-systems like SWNTs and graphene by employing Raman and electronic absorption spectroscopy. There are some reports in the literature on the chemical doping of SWNTs by I_2 and Br_2 ,[114, 115] but the spectroscopic changes associated with the accompanying charge-transfer interaction have not been properly delineated or explained. Interaction of single layer and bilayer graphenes with I_2 and Br_2 have been reported recently,[116] even though graphite intercalation compounds of halogens have been studied extensively.[117]

In this chapter, we describe the results of our detailed studies on the interaction of SWNTs and graphene with different halogen molecules probed by first-principles calculations. We also presented a breif report of the corresponding results obtained by the experiment probed by spectroscopy. In the experiment, as-prepared SWNTs produced by the arc-discharge method are subjected to interaction with halogen(Br_2 and I_2)and interhalogen molecules (ICl and IBr) which would have different electron affinities, the expected order being $ICl>Br_2>IBr>I_2$ based on electronegativity considerations. The halogens are expected to p-dope SWNTs to varying degrees. The halogen-doped samples are characterized using Raman and electronic absorption spectroscopy. Few layer graphene (FLG) prepared by the exfoliation of graphite oxide and arc-discharge methods are also interacted with the halogens and the samples studied by spectroscopic methods. The changes in the spectroscopic signatures of both these nanocarbons are found to depend on the level of doping and also on the varying electron-withdrawing ability of the halogens. These experimental findings have been rationalized by ab-initio DFT investigations.

2.2 Computational Details

All the electronic structure and energetic calculations are performed using the linear combination of atomic orbital density functional theory (DFT) within the generalized gradient approximation (GGA), considering the Perdew – Burke – Enzerhof (PBE) [118] exchange and correlation functional and using the double zeta polarized basis set (DZP) for all atoms as implemented in the SIESTA package. [119] Although, it is known that DFT poorly describes dispersion forces for the physisorption of the molecules, the molecules under consideration, owing to their lack of π-surface, render dispersion forces less important and hence the qualitative estimations of the obtained results wouldn't change much. This is evident from the large number of studies involving the same method for gas molecule adsorption in the literature. [109, 110, 120-123] It should also be noted that local density approximation (LDA) overestimates the adsorption energy [124] for the weakly bound charge transfer systems and hence, we believe that GGA is an appropriate choice for our calculations describing the interaction between the halogens and the nanocarbons.

We have considered the norm conserving pseudo potentials [125] in the fully non-local Kleinman – Bylander form [126] and are constructed from 7 valence electrons for all the halogens. A real space mesh cut off of 400 Ryd is used for both graphene and SWNTs. For complete relaxation and for structural relaxation, a Monkhorst k-point grid of 1×1×20 and 12×12×1 are used, respectively for systems involving SWNTs and graphene. Systems are considered to be relaxed when the forces acting on all the atoms are less than 0.04 eV $Å^{-1}$. A large vaccum separations are used to supress spurious interactions in the non-periodic direction. We have considered graphene in the xy-plane and to create a sufficient vacuum along the z-direction a translation vector of 25 Å is considered to ensure the energy convergence. In the case of SWNTs, translational vectors of 25 Å are considered along x and y directions to avoid unwanted interactions. We separately relaxed the structures of pristine graphene (52 atoms) and SWNT (66 and 62 atoms for semiconducting and metallic, respectively), halogen molecules and also halogen-nanocarbon-complex supercells at the same level of calculation.

2.3 Results and Discussion

2.3.1 Experimental

Halogen doping causes pronounced changes in the DOS near the Fermi level of the SWNTs as verified by the changes in the Raman spectra of the doped samples in comparison to those of pristine SWNTs. Raman G-band of iodine monochloride (ICl) doped SWNTs is stiffened in comparison to that of the as-synthesized sample. As the concentration of ICl in the doped sample is increased, the G-band of the SWNTs shifts to higher wavenumbers (see figure 2.1a) and there is a progressive decrease in the intensity of the 1540 cm^{-1} feature relative to the G-band maximum.

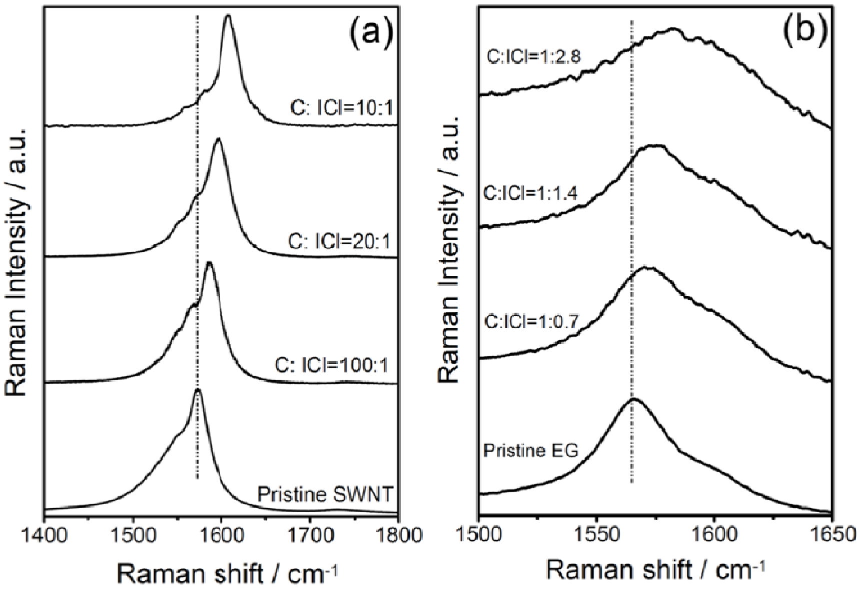

Figure 2.1 Changes in the G-band in the Raman spectra of (a) SWNT, and (b) graphene as the concentration of doping with ICl is varied.

The extent of G-band shift varies with the magnitude of doping and the halogen molecule. The G-band stiffening follows the general order of I_2 < IBr < Br_2 < ICl which is consistent with the expected order of electron affinities of the halogen molecules. Higher the electron affinity of the halogen molecule (ICl in the present case), higher is the G-band shift from that of the pure SWNT. In the case of graphene, the G-band stiffening with increase in the ICl content is not as marked as in case of SWNTs (see figure 2.1b). Also, the G-band of FLG does not show marked changes on doping with different halogens as in the case of SWNTs. Electron absorption spectroscopy results supported the Raman spectroscopy results.

2.3.2 Theoretical

For a microscopic understanding of these experimental results, we have performed ab-initio DFT computations on the various halogen-nanocarbon-complexes. The details of the calculations are provided in the computational methods. In case of SWNTs, the theoretical studies are performed on model metallic (5, 5) and semiconducting (8, 0) nanotubes. Adsorption energies of the different halogen-nanocarbon-complexes are calculated to understand their relative stability. The adsorption energy per adsorbate molecule is calculated as the energy difference between the optimized total energy of the halogen-nanocarbon-complex and the individual optimized energies of the halogen molecule and the pristine nanocarbon.

$$E_{\text{(adsorption)}} = E_{\text{(halogen-nanocarbon-complex)}} - E_{\text{(halogen molecule)}} - E_{\text{(pristine nanocarbon)}} \qquad (2.1)$$

Table 2.1 Adsorption energy and optimized distance (between nanocarbon and X_2) of X_2 adsorbed nanocarbons

	CNT (5, 5)		**Graphene**		**CNT (8, 0)**	
Molecule	**Equilibrium distance (Å)**	**Adsorption energy (eV)**	**Equilibrium distance (Å)**	**Adsorption energy (eV)**	**Equilibrium distance (Å)**	**Adsorption energy (eV)**
Br_2	3.03	-2.00	2.81	-1.88	2.82	-1.87
IBr	3.07	-1.82	3.06	-1.71	2.83	-1.70
I_2	3.27	-1.09	3.05	-1.52	3.05	-1.54
ICl	3.18	-1.10	3.09	-1.01	3.16	-0.98

The various adsorption parameters concerning the different halogen-nanocarbon-systems viz. adsorption energies and equilibrium distances of separation between nanocarbons and adsorbed halogens are presented in Table 2.1 and the corresponding optimized structures are shown in Figure 2.2. The stronger the interaction between the halogens and the nanocarbons, the greater will be the

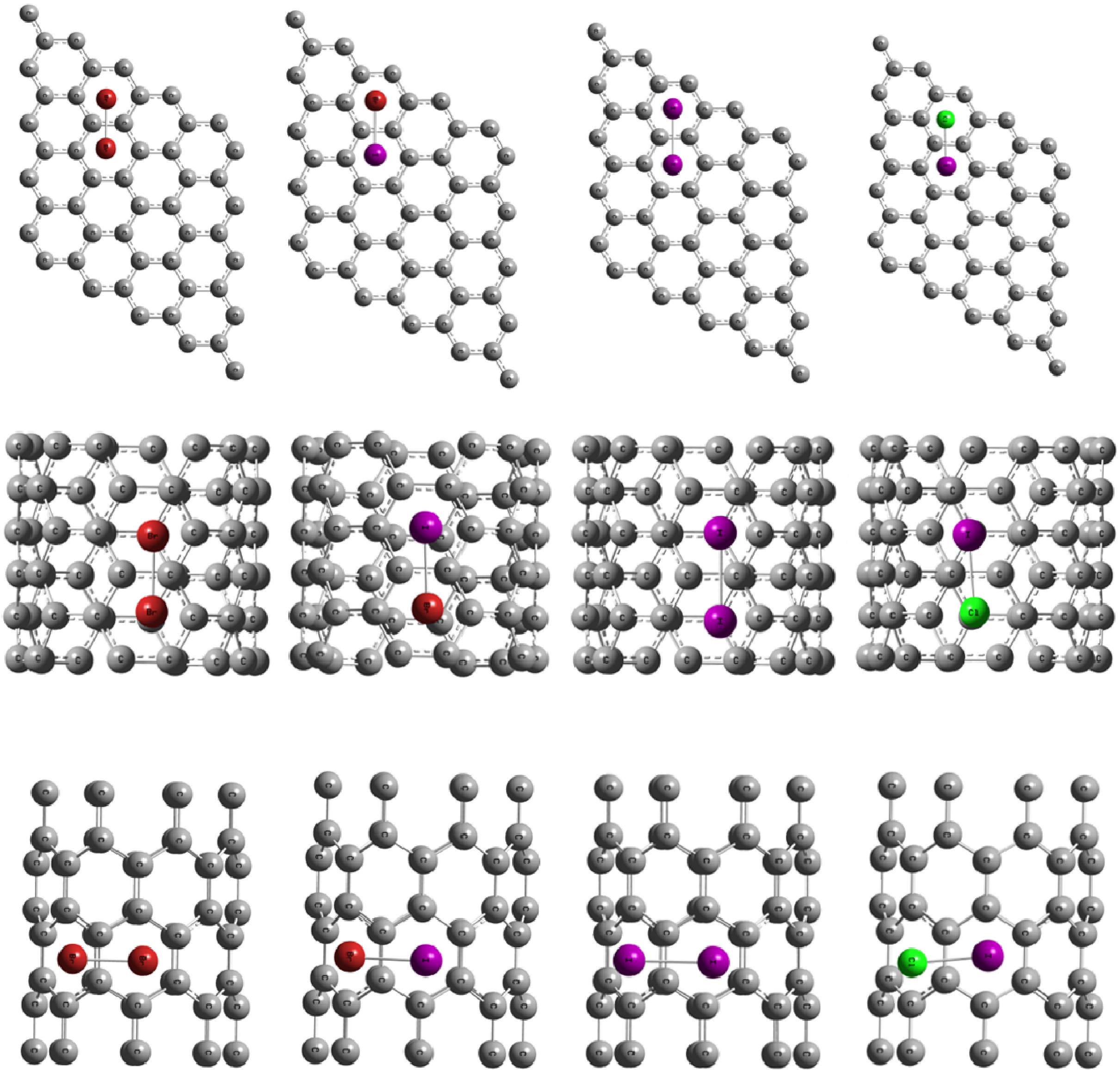

Figure 2.2 Optimized halogen adsorbed nanocarbons. From top to bottom graphene, CNT (5, 5), CNT (8, 0), respectively and from left to right Br_2, IBr, I_2, ICl adsorbed nanocarbons, respectively.

adsorption energy of the complex. As is evident from Table 2.1, all the adsorption energy values are in the range of ~ 1 – 2 eV (23 – 46 kcal mol^{-1}) which clearly indicates that the halogen molecules are physisorbed on nanocarbon surfaces, the equilibrium distances of adsorption being of the order of ~ 2.8 Å to ~ 3.3 Å. It can also be envisaged from Table 2.1 that the order of adsorption energy is same for all the halogen molecules (for both the nanocarbons), Br_2 being the strongest adsorbate and ICl being the weakest one. To identify the feasible reason for the general order of halogen-nanocarbon interaction energies (i.e. Br_2 > IBr > I_2 > ICl according to Table 2.1), the adiabatic electron affinities of the various halogen molecules are calculated using the same level of theory as mentioned earlier. The order of electron affinities is found to be exactly similar to the order of interaction energies i.e. Br_2 > IBr > I_2 > ICl, which leads us to conclude that higher the electron affinity of the halogen greater will be its interaction with the nanocarbon. Interestingly, the adsorption energies of most of the halogens to the nanocarbons follows the order CNT (5, 5) > Graphene > CNT (8, 0). This indicates that the extent of interaction of a halogen to the nanocarbons increases in the order semiconducting < semi-metallic < metallic i.e. in the order of abundance of electrons in the nanocarbon. Thus, from the order of adsorption energies of the halogens with different nanocarbons, we find that molecules with higher electron affinities interact strongly to the electron rich nanocarbons. From Mülliken population analysis, we find that the extent of charge transfer is relatively small (only ~ 0.2 % charge transfer is observed). We also calculated the first ionization energies of all the molecules using same level of theory, to compare the electron donating capability of the molecules and we find that the electron donating order is I_2 > IBr > Br_2 > ICl.

To understand the effect of halogen adsorption on the electronic properties of nanocarbons, the band diagrams and the corresponding density of states (DOS) are plotted together with the projected DOS (PDOS) for all the systems as shown in figures 2.3, 2. 4, 2.5 for Graphene, CNT (5, 5) and CNT (8, 0) respectively. Halogen adsorption changes the DOS of graphene (figure 2.3) near the Fermi energy significantly, whereas, for the case of CNT (8, 0) and CNT (5, 5) changes are comparatively lesser (figures 2.4 and 2.5). We also find that the energy band gap of nanocarbons changes upon halogen adsorption and the changes follow the same order as the electron affinity of the halogen molecules for SWNTs (i.e. Br_2 > IBr > I_2 > ICl) but for graphene it follows the ionization energy order. Moreover, the linear band dispersion behavior at the Fermi level in pristine graphene is destroyed with a generation of energy band gap (in the order of ~ 0.088 eV to 0.27 eV) at the Fermi level after the adsorption of molecular species. Near the Fermi level there are discrete molecular bands which are essentially a superposition of bands from both the graphene and that of the adsorbate, with larger contribution from adsorbed molecules, as can be seen from the DOS and PDOS of the complexes (figure 2.3). In case of SWNTs (i. e. for both (8, 0) and (5, 5)), there is a change in the band structure near the Fermi level (see fig 2.4, 2.5) due to the presence of adsorbed molecules which is not so pronounced in the case of graphene. Compared to the pristine semiconducting SWNT (8, 0), some extra bands are found to originate slightly below the Fermi level for X_2 adsorbed CNT (8, 0). These energy levels arise from the adsorbed molecules as illustrated in the projected density of states of these particular complexes. Band structure for the halogen adsorbed SWNT (5, 5), however, doesn't change much near the Fermi level.

The Fermi energy shifts for the nanocarbons upon halogen adsorption follow exactly the same trend for both the nanocarbons viz. I_2 > IBr > Br_2 > ICl which is in accordance with the electron donating capability of the halogen species. This can be explained on the basis of the fact that as the electrons are added to the conduction band, there should be an upward shift in the Fermi energy, which essentially is what we observed. Iodine has less ionization energy (or more electron donating capability) and hence the Fermi energy shift is more for iodine adsorbed nanocarbons.

The order of the shifts in the Fermi energy for other molecules can be explained in a similar manner. It is well known that [81, 100, 109, 114, 116, 127, 128] greater the amount of charge transferred (to) from the nanocarbon greater will be the (softening) stiffening of the G-band. In accordance with the above argument for the order of Fermi energy shift, iodine should stiffen the G-band less as compared to others and iodine monochloride should stiffen the G-band more and the order should be ICl > Br_2 > IBr > I_2 which qualitatively matches with the experimental G-band shift for SWNTs. Electron affinity order obtained for these molecules, supports the above shift in G-band order (except for ICl). The electron affinity order obtained from theoretical calculations is Br_2 > IBr > I_2 > ICl and the experimental G-band stiffening varies in the order ICl > Br_2 > IBr > I_2. Thus, the order of electron affinity matches with that of experimental G-band stiffening.

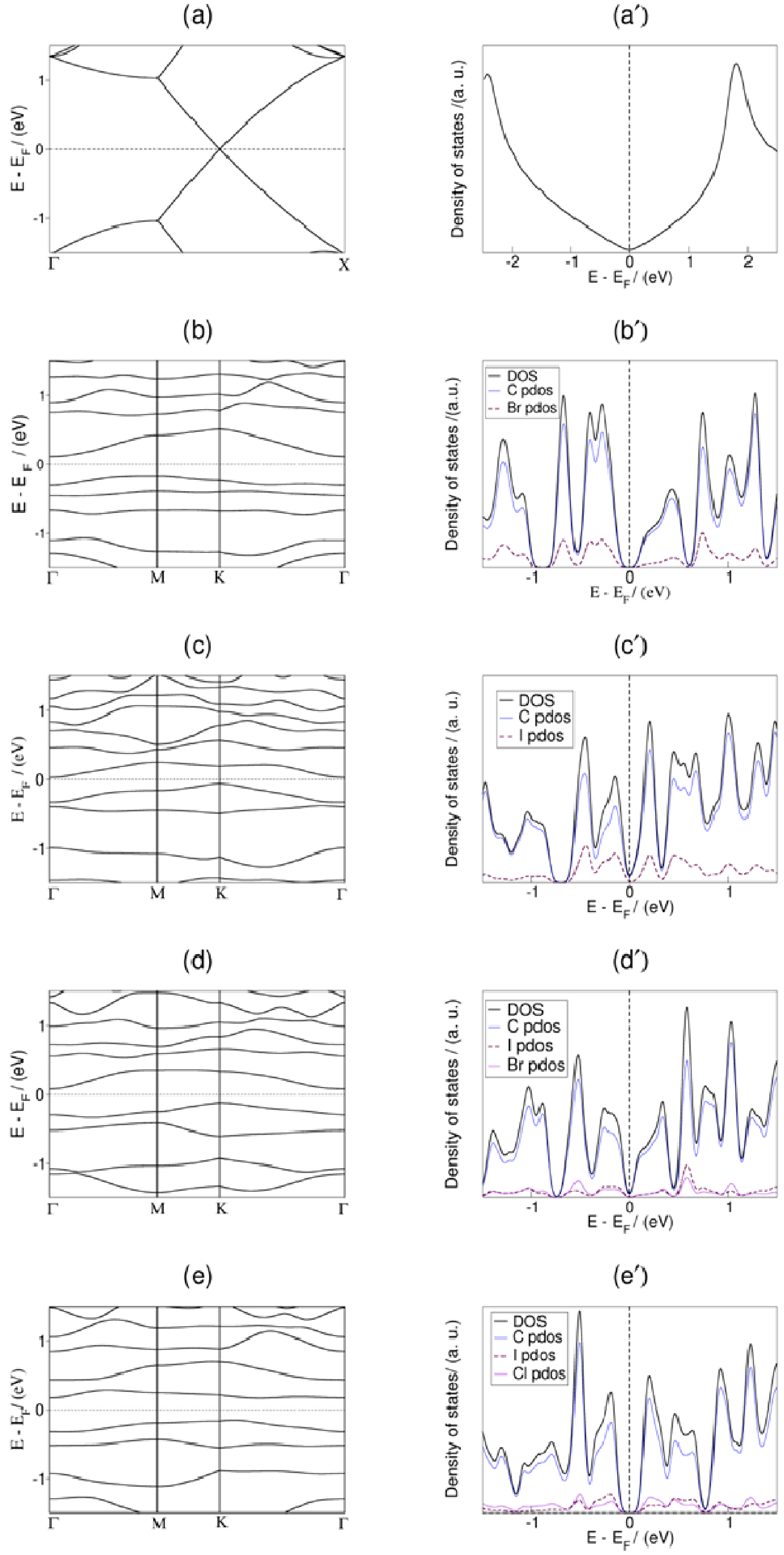

Figure 2.3 Electronic band structure of (a) Pristine graphene (b) Br_2 adsorbed graphene (c) I_2 adsorbed graphene (d) IBr adsorbed graphene (e) ICl adsorbed graphene. Electronic DOS of (a') Pristine graphene (b') Br_2 adsorbed graphene (c') I_2 adsorbed graphene (d') IBr adsorbed graphene (e') ICl adsorbed graphene.

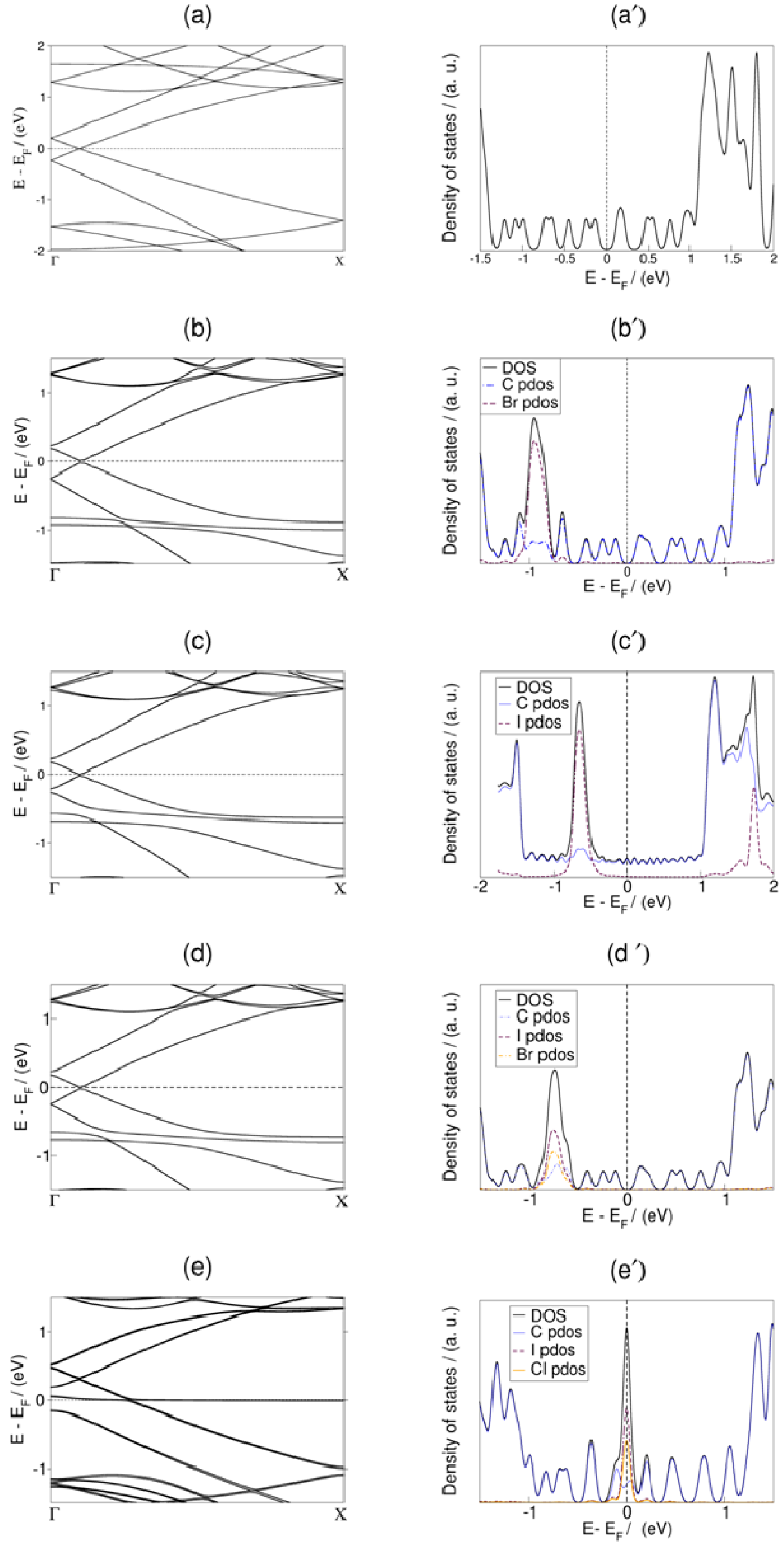

Figure 2.4 Electronic band structure of (a) Pristine CNT (5, 5) (b) Br_2 adsorbed CNT (5, 5) (c) I_2 adsorbed CNT (5, 5) (d) IBr adsorbed CNT (5, 5) (e) ICl adsorbed CNT (5, 5). Electronic DOS of (a’) Pristine CNT (5, 5) (b’) Br_2 adsorbed CNT (5, 5) (c’) I_2 adsorbed CNT (5, 5) (d’) IBr adsorbed CNT (5, 5) (e’) ICl adsorbed CNT (5, 5).

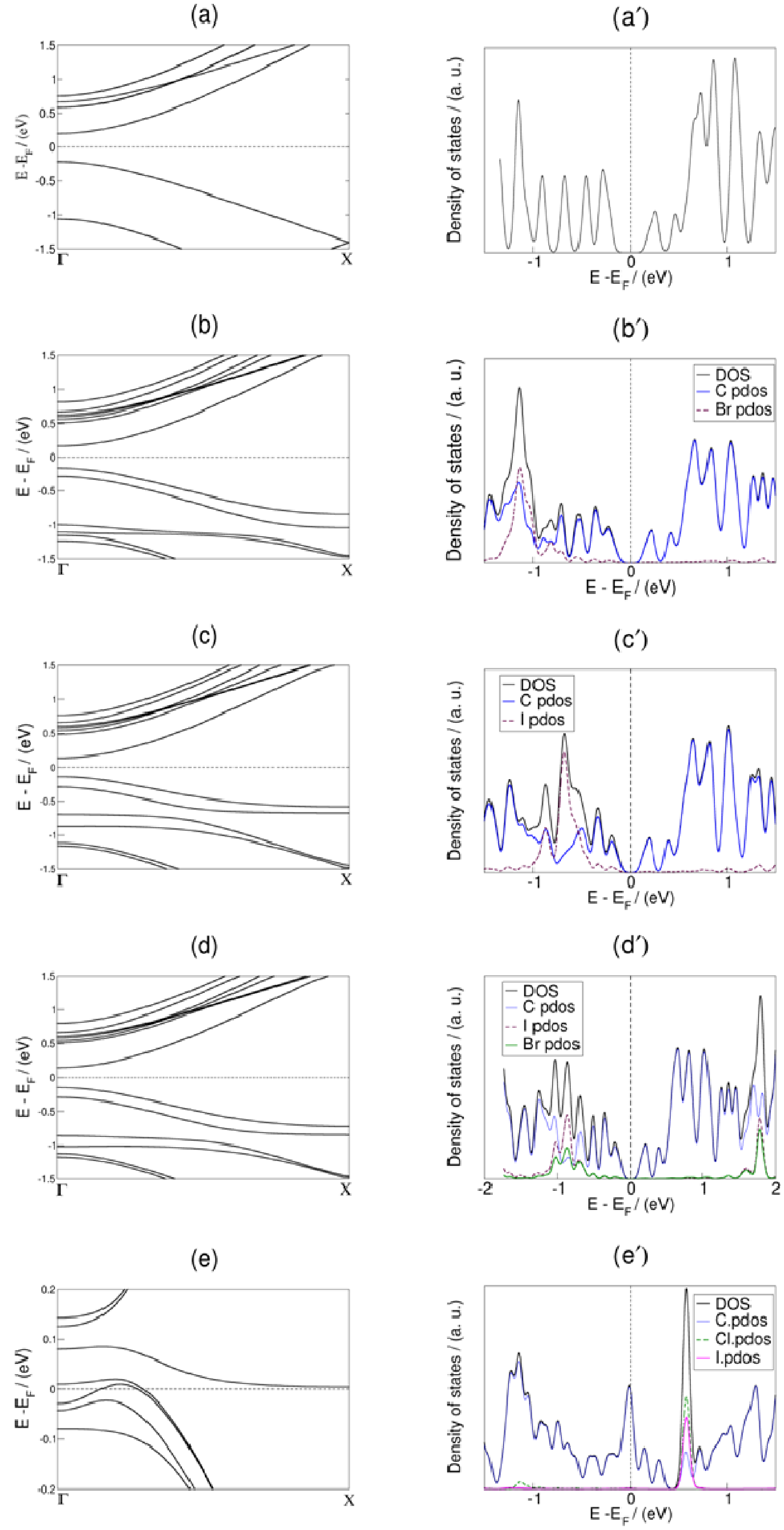

Figure 2.5 **Electronic band structure of (a) Pristine CNT (8, 0) (b) Br_2 adsorbed CNT (8, 0) (c) I_2 adsorbed CNT (8, 0) (d) IBr adsorbed CNT (8, 0) (e) ICl adsorbed CNT (8, 0). Electronic DOS of (a′) Pristine CNT (8, 0) (b′) Br_2 adsorbed CNT (8, 0) (c′) I_2 adsorbed CNT (8, 0) (d’) IBr adsorbed CNT (8, 0) (e’) ICl adsorbed CNT (8, 0).**

Interestingly, both CNT (8, 0) and CNT (5, 5) ICl adsorption leads to a finite DOS at the Fermi level. From the PDOS of ICl adsorbed CNT (5, 5) (fig 2.4) one can notice that there is a significant contribution from the iodine and chlorine atoms to the DOS at the Femi energy for this complex, thus results in a metallic behavior. Unlikely, for the case of CNT (8, 0) the contribution to the DOS at the Fermi energy mainly comes from the carbon atoms. The reason for the metallicity could be mainly because of the structural distortion and the presence of the DOS of adsorbate or of carbon at the Fermi energy rather than the charge transfer, because, the change in the charge of the nanocarbons is very insignificant (only 0.2 %) to account for such a huge change in band structure.

2.4 Conclusions

In conclusion, doping by molecular charge-transfer induced by interaction of different halogen molecules with SWNTs and few-layer graphene has been investigated. The spectroscopic signature of doping is more pronounced in case of SWNTs than with graphene. Adsorption energy values, obtained from theory, clearly indicates that the halogen molecules are physisorbed on nanocarbon surfaces and higher the electron affinity of the halogen the greater is its interaction with the electron rich nanocarbon. The Fermi energy shifts for the nanocarbons upon halogen adsorption follow exactly the same trend for both the nanocarbons and the order of the expected G-band shift from theory, obtained using the calculated electron affinity values and Fermi energy shifts, matches qualitatively with the experimental G-band shift for SWNTs.

The varying electron withdrawing ability of the different halogens (manifested by their electron affinity) produces differences in the spectral properties of doped samples of both SWNTs and graphene which are confirmed by the theoretical results. On an average, the observed changes in the Raman spectra of SWNTs and graphene brought about by the halogens confirm to the order of, $ICl>Br_2>IBr>I_2$. Hence, theoretical calculations supported the experimental studies.

Chapter 3

Computational Studies on Structural and Excited State Properties of Chlorophyll F with Various Axial Ligands

3.1. Introduction

Chlorophylls (chls) are the essential light harvesting pigments of photosystems present in the thylakoid membrane of plants, algae and cyanobacteria. [82, 129] Five chemically distinct chlorophylls are known from oxygenic photosystems, termed as chl a, chl b, chl c, chl d and chl f (see figure 3.1), which absorb solar light at different wavelengths and convert it into chemical energy. [130, 131] All chls contain a chlorin ring with Mg at its centre, (bonded to the nitrogens of the four pyrrole units present in the chlorin ring) and they differ from each other by their substituents R, R′, R″ as shown in figure 3.1. These substituents affect the π– electron conjugation of the chlorin ring, and thus lead to different absorption spectra. [86]

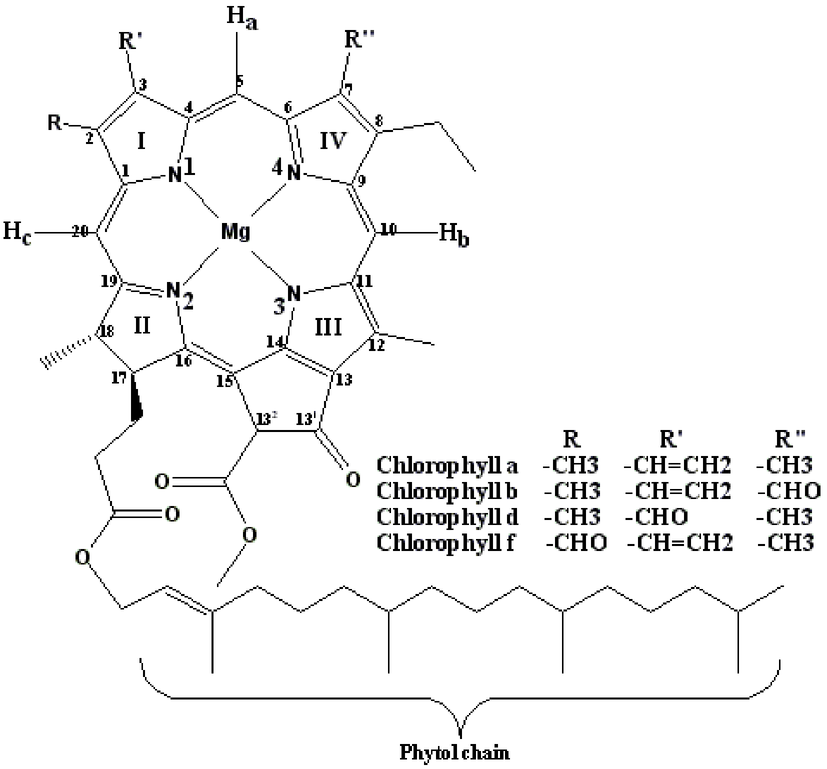

	R	R'	R''
Chlorophyll a	-CH3	-CH=CH2	-CH3
Chlorophyll b	-CH3	-CH=CH2	-CHO
Chlorophyll d	-CH3	-CHO	-CH3
Chlorophyll f	-CHO	-CH=CH2	-CH3

Figure 3.1 Schematic representations of chemically distinct chlorophylls. Numbering scheme used in this chapter is shown.

Important peaks of the absorption spectra of chls include low energy Q_y bands and high energy B_x and B_y bands. The Q_y absorption wavelengths of the chls are: chl *a* (665 nm), chl *b* (652 nm), chl *d* (696 nm) and chl *f* (706 nm). [130, 132-134] Among all these chls, the Q_y absorption maximum of chl *f* is red–shifted and it is in the infrared (IR)–region. Chen *et. al.,*[134] discovered chl *f* from cyanobacteria and reported preliminary structural and spectroscopic studies. However, they did not focus on the reason behind this huge red–shift in the Q_y band of chl *f*, when compared with other chls. The present study is done to understand the underlying cause for this red–shift. It is also important because this indicates that the chl *f* can perform "oxygenic photosynthesis" in low light conditions.

Though all chls are interesting, our study only focuses on chl *f* and its structural isomer chl *b*. Chl *b* and chl *f* structurally differs from each other only by the position of – CHO group (see figure 3. 1). This makes the system interesting for electronic structural studies, because just by changing the position of a functional group, there is a huge shift in the Q_y band (54 nm). To understand the reason behind such a huge shift we have employed the theoretical methods such as DFT and TDDFT.

To determine the structure of a chl within the complex protein environment is a vast challenge. In many chl proteins, the Mg–atom exhibits penta-coordination, [135, 136] where the fifth coordination may be with an amino acid residue or with a water molecule. There are a few theoretical papers which considered the effects of axial ligation in chl *a*. [85, 137-139] To our knowledge no work has been done on the affect of axial ligation to chl *f*. The present study focuses on the structural and excited state properties of chl *f* in the presence and absence of axial ligands (such as Histidine, Aspartate, Serine, Tyrosine and water). The obtained structural changes are well supported by the computed NMR results. We also have studied the redox potentials of these molecules, since chls in photosystem are involved in electron transfer.

In what follows, we have given the details of our computational methods and how we modelled our systems in section 3.2. Structural differences among chl *f*, chl *b* and chl *a* are reported, along with the structural changes in chl *f* upon axial ligation, in sections 3.3.1 and 3.3.2. Redox properties are discussed in section 3.3.3. Section 3.3.4 is devoted to the changes in the absorption spectra among different chl molecules, in particular, the reasons for the red–shift in chl *f*, followed by the conclusions in section 3.4.

3.2. Computational Details

Initial structures of chl *f* and chl *b* are created from the XRD structure of chl *a* presented at 2.5 Å resolutions (1JBO.pdb). [140] The long phytol chain attached to the pyrrole ring II is modelled as –

CH_3 group in order to reduce the computational cost (see figure 3.1). Removal of phytol chain is considered as a reasonable approximation from several previous computational studies on chl *a*. [85, 137-139, 141, 142]

As there are two conformers possible with respect to the –CHO group for chl *f* and chl *b*, geometry optimizations are performed to find the conformer with minimum energy and this minimum energy conformer is considered for further calculations. Five neutral axial ligands are considered in our study. 'Histidine' is modelled as "Imidazole", 'Aspartate' as "CH_3COOH", 'Serine' as "CH_3OH", 'Tyrosine as "Phenol" and 'water' as "H_2O". These are the axial ligands which occur frequently in photosystems of cyanobacterium. [85]

All the geometry optimizations and energy calculations are performed with the Density Functional Theory (DFT). The three–parameter hybrid functional B3LYP (Beke exchange with Lee, Yang and Parr correlation) [143-145]with 6–31+G (d) basis set is used for all the atoms as implemented in the Gaussian 03 program package. [146] We choose the B3LYP functional, because, it is found to be one of the appropriate functional [85, 137-139, 141, 142] for the prediction of electronic structure for the various oxidation states of chls. We are aware that this DFT functional is not fully adequate to describe the long–range dispersion forces or stacking interactions, but, we do not expect them to play an important role in the single unit chl molecule investigated here. The computed energies are corrected for basis set superposition error (BSSE) using counterpoise method. [147, 148]All the molecular properties are calculated at the same level of theory and using the Gaussian 03 program package. [146] ^{1}H–NMR chemical shielding values are calculated using Gauge Including Atomic Orbital (GIAO) method. [149-153] Time Dependent DFT (TDDFT) [154, 155] is used to calculate the absorption properties of the optimized geometries.

In this work we did not include the implicit solvent effect, since it is already proven that in the continuum model, solvent effect on the neutral ligated chl *a* molecules are negligible [85] and the initial molecular structures are obtained from 1JBO.pdb crystal structure, where all environmental effects have implicitly been included. In addition, it is known that in the protein environment, the inter–molecular H–bonding interaction between axial ligands and the surrounding environment will be dominant, which cannot be mimicked using implicit solvent model. To use an explicit solvent will be expensive and hence, in this work we report only the gas phase results.

3.3 Results and Discussions

3.3.1 Structural Changes

In this section we discuss the structural differences among chl *f*, chl *a* and chl *b* along with a structural comparison between the two conformers of chl *f*. In addition, structural changes due to axial ligation are also discussed.

Table 3.1 Computational and experimental ^1H NMR chemical shift values (*ppm*) for the H_a, H_b, H_c and formyl hydrogen atoms for the various Chls studied in this paper. Hydrogen labelling schemes are shown in the figure 3.1.

Molecule	Method	H_a	H_b	H_c	Formyl hydrogen
Chl *a*	Computational	9.28	9.67	8.51	——
	Experimental[156]	9.29	9.54	8.32	——
Chl *b*	Computational	10.93	9.48	8.17	11.35
	Experimental[157]	10.04	9.64	8.20	11.22
Chl *b*′	Computational	9.73	9.71	8.31	11.83
Chl *f*	Computational	9.60	9.57	10.17	11.51
	Experimental[134]	9.79	9.86	9.77	11.35
Chl *f'*	Computational	9.84	9.64	8.95	11.71
H_2O	Computational	9.57	9.54	10.20	11.55
His	Computational	9.60	9.48	10.15	11.49
Ser	Computational	9.59	9.63	10.09	11.45
Asp	Computational	9.44	9.66	10.21	11.16
Tyr	Computational	9.43	9.77	10.15	11.17

Among the many conformers of chl *b*, the two conformers, S–cis chl *b* (chl *b'*) and S–trans–chl *b* (chl *b*) are reported to be more stable and close in energy. [142, 158] We have found the same, where the S–trans conformer turns out to be more stable than S–cis conformer only by 5 kcal mol^{-1}, and hence, both conformers can be present in the gas phase. However, one of the conformer might be stabilized in the protein environment due to the presence of an inter–molecular hydrogen bonding interaction. In order to find the conformer present in the nature, the chemical shift values of formyl–^{1}H for both conformers are computed. Chemical shift value of S–trans chl *b* (11.35 *ppm*) is comparable with experimental value of chl *b* (11.25 *ppm*) (see table 3.1), than the S–cis chl *b* (11.85 *ppm*). In addition, the computed values are also in good agreement with the already reported values using CAM–B3LYP functional. [142]

Similarly, S–trans conformer of chl *f* is found to be stable by 1 kcal mol^{-1} than the S–cis conformer and the chemical shift value of formyl group for S–cis (11.71 *ppm*) and S–trans (11.51 *ppm*) conformers of chl *f* and experimental value (11.35 *ppm*) of chl *f* (see table 3.1) shows that the S–trans conformer chemical shift value is more comparable with experimental value. [134] The small difference between the experimental and computational value is due to the absence of protein and water environment. The above studies provide us an evidence that chl *b* and chl *f* might be present in the S–trans conformation in protein environment, and are considered for further studies reported in this chapter.

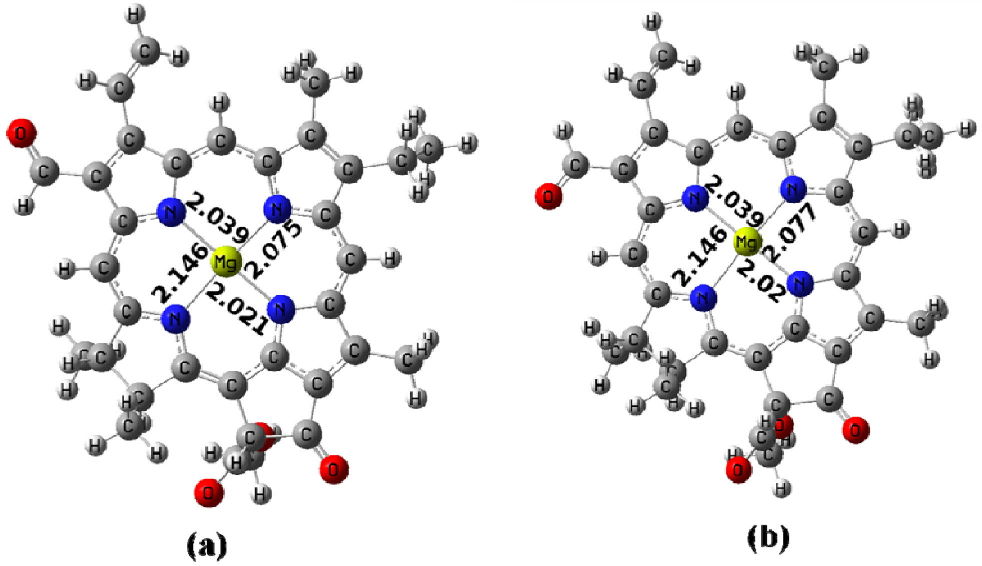

Figure 3.2 Optimized geometry of two stable conformers of Chl f (a) S–cis chl f (b) S–trans chl f. Important bond distances are shown in Å. Note that the Mg present in the plane of macrocycle.

In the optimized structure of chl *f*, Mg is in the plane of the chlorin macrocycle, and is coordinated asymmetrically to the four pyrrole nitrogens. The order of the Mg–N distances are Mg–N2 (2.146 Å) > Mg–N4 (2.077 Å) > Mg–N1 (2. 039 Å) > Mg–N3 (2.020 Å), (see table 3.2) which is similar to the order observed for other chls. [85, 137-139, 141, 142] Longer distance of Mg–N2 is because of the saturation of the corresponding pyrole ring (ring II).

The affect of the functional groups (R, R′ and R″) on chlorin ring can further be understood by comparing the structure of chl *f* with chl *a* and chl *b* (see figure 3. 1). The affect of the changes in the functional groups are clearly reflected in the Mg– N1 and Mg–N4 bond distances and ^{1}H–NMR chemical shift values of H_a and H_c as shown in the tables 3.1 and 3.2. The Mg–N1 bond of chl *f* (2.039 Å) is longer than that of the Mg–N1 bond in Chl *a* (2.033 Å) and Chl *b* (2.030 Å), due to the presence of the electron withdrawing –CHO substituent at the corresponding pyrole ring (ring I) of chl *f* (see table 3.2). Presence of the – CHO substituent at ring I in chl *f* is also the reason for the downfield shift of H_c by 1.66/2.00 *ppm* when compared to chl *a* /chl *b*. Similarly, the presence of –CHO group at ring IV in chl *b* results in longer Mg–N4 bond (2.083 Å) than chl *f* (2.077 Å) and chl *a* (2.070 Å) (see table 3.2). In addition, ^{1}H–NMR chemical shielding value of the H_a of chl *b* is shifted downfield by 1.33/1.65 *ppm* when compared to the H_a hydrogen of the chl *f* /chl *a*. (see table 3.1)

The above mentioned results provide an evidence for the most possible chl *f* conformer in the gas phase. However, the Mg atom of chl *f* could be penta–coordinated in protein environment, as observed earlier in chl *a* and chl *b*. [85, 138, 139, 159-161] As mentioned in the computational section, we have considered five neutral ligands for our studies. Coordination of Mg with neutral ligands does not change the order of Mg–N bond distances: Mg–N2 > Mg–N4 > Mg–N1 > Mg–N3 (see table 3.2), however, Mg–N bonds are elongated by 0.01–0.04 Å and Mg atom is displaced from the plane of the macrocycle by 0.2 – 0.4 Å (see figure 3.3). The amount of the displacement of Mg atom is shown by computing out of plane distance (d_{OOP}) by,

$$d_{OOP} = [\mathrm{Cos}\ (\theta/2) * (d_1+d_3)] / 2,$$

where, θ is the N1–Mg–N3 bond angle; d_1 = Mg–N1 bond distance; and d_2 = Mg–N3 bond distance.

d_{OOP} distances of Mg are in the order: Mg–His [Mg–N] (0.3681 Å) > Mg–Ser [Mg–O] (0.270 Å) > Mg–Tyr [Mg–O] (0.258 Å) ≈ Mg–Asp [Mg–O] (0.254 Å) > Mg–H_2O [Mg–O] (0.242 Å). d_{OOP} distance highly depends on the steric hindrance of the ligated atom (see table 3.2). There is one exception from the trend, Ser, for which d_{OOP} distance is larger than Tyr and Asp. This is due to orientation of CH_3 group of serine, which is very close to macrocycle (see figure 3. 3d).

Table 3.2 Computed important bond distances (Å) and Mulliken charges (e) for chl *a*, chl *b*, chl *b′*, chl *f*, chl *f′*, neutral ligand ligated chl *f* and negative charge ligand ligated chl *f*.

Molecules	**Mg–N1**	**Mg–N2**	**Mg–N3**	**Mg–N4**	**Mg–ligand**	**d_{OOP}**	**Mulliken atomic charge**	
							Mg	**Ligated atom**
Chl *a*	2.033	2.150	2.020	2.074	–	0.019	0.841	–
Chl *b*	2.030	2.149	2.021	2.083	–	0.026	0.861	–
Chl *b′*	2.029	2.151	2.019	2.083	–	0.024	0.822	–
Chl *f*	2.039	2.146	2.020	2.077	–	0.024	0.818	–
Chl *f′*	2.039	2.146	2.021	2.075	–	0.022	0.802	–
H_2O	2.058	2.166	2.044	2.108	2.169	0.242	0.419	–0.843
His	2.076	2.197	2.058	2.120	2.190	0.368	–2.042	–0.274
Ser	2.067	2.183	2.042	2.102	2.139	0.270	–0.512	–0.467
Asp	2.058	2.168	2.031	2.094	2.246	0.224	–1.233	–0.431
Tyr	2.066	2.174	2.035	2.100	2.191	0.258	–1.391	–0.473
Negatively charged ligands								
Ser^{-}	2.106	2.24	2.075	2.136	1.953	0.536	–0.2438	–0.076
Asp^{-}	2.119	2.326	2.082	2.159	1.964	0.616	–0.269	–0.219
Tyr^{-}	2.086	2.211	2.068	2.128	2.02	0.485	–1.437	–0.084

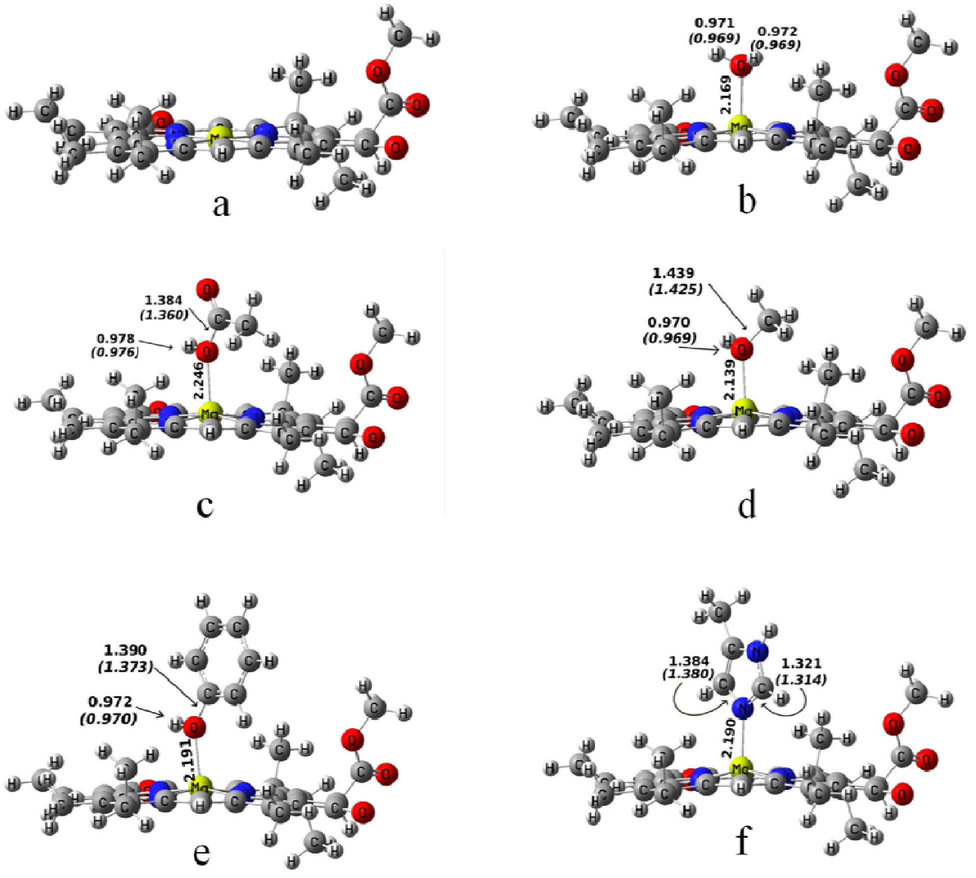

Figure 3.3 Optimized geometry of (a) Chl f, axial ligated (b) H_2O, (c) Asp, (d) Ser, (e) Tyr and (f) His chl f molecules. The displacement of Mg from the plane (d_{OOP}) is shown. Important bond distances are shown in Å. Distances of the respective bonds in the bare ligands are shown in brackets and Italic.

Mg–axial ligand distances are in the order: Mg–Asp [Mg–O] (2.244 Å) > Mg–His [Mg–N] (2.190 Å) ≈ Mg–Tyr [Mg–O] (2.190 Å) > Mg–H_2O [Mg–O] (2.168 Å) > Mg–Ser [Mg–O] (2.139 Å). The ligated oxygen atoms of Asp, Tyr molecules are attached to the acidic hydrogen, which increases Mg–O bond distances compared with Mg–OH_2 distance. However, the larger electrostatic repulsion between the CH_3 hydrogen and chlorin macrocycle decreases the Mg–O bond distance in chl *f*–Ser (see figure 3. 3) by distorting Mg atom from its plane. The effect of the presence of acidic hydrogen can be further explained by calculating the Mg–O bond distances for negatively charged Tyr ($C_6H_5O^-$), Asp (CH_3COO^-), Ser (CH_3O^-) ligands. The Mg–O bond distances are in the order: Mg–Tyr^- (2.02 Å)> Mg–Asp^- (1.96 Å) > Mg–Ser^- (1.95 Å) (see table 3.2), which are smaller than the Mg–OH_2 (2.169 Å) bond distance.

Computed Mg–N, d_{OOP}, Mg–Ligand bond distances of axial ligated chl *f* and chl *a* molecules [85] follow the same trend, except that these bond distances are shorter in chl *f* by 0.01–0.03 Å. These results show that, axial ligation to chl *f* affects the macrocycle unit similar to that in chl *a*.

Additionally, axial ligation to chl *f* follow the similar trend of the chemical shielding values as in chl *f*, *i.e.*, the formyl hydrogen is always in downfield when compared to the H_a, H_b and H_c. But, there are small changes in the chemical shielding values depending upon the orientation of the axial ligands. The presence of electron donating neutral axial ligands shifted the chemical shielding values of H_a, H_c, formyl hydrogens by 0.02–0.35 *ppm* towards upfield (see table 3.1) and H_b by 0.03–0.20 *ppm* towards downfield. There are three exceptions from this trend.

(i) The inter–molecular hydrogen bonding interaction between H_2O and formyl group is the reason for the downfield shift in formyl, H_c and the upfield shift in H_b proton.

(ii) The orientation of His shifts the H_b chemical shielding value towards upfield and

(iii) The H-bonding interaction between the acidic hydrogen of Asp and –CHO is the reason for the downfield shift in the H_c.

Table 3.3 Computed reduction potential (RP1, RP2 in eV) and BSSE corrected Mg–ligand bond dissociation energies (E_{BDE}, KJ mol^{-1}) for chl f and axial ligated chl f.

Molecules	**RP1 = E (N - 1) –E (N) - 4.43** **eV**	**RP2 = E (N) – E (N + 1) - 4.43** **eV**	**BSSE corrected E_{BDE}** **KJ mol^{-1}**
chl *f*	2.073	–2.199	0.000
H_2O	1.910	–2.253	–45.263
His	1.665	–2.471	–70.704
Ser	1.856	–2.308	–48.624
Asp	2.019	–2.144	–25.654
Tyr	1.883	–2.253	–34.184

3.3.2 Bond Dissociation Energy (E_{BDE}) of Axial Ligated Chl *f*

Mg–ligand bond dissociation energy (see table 3.3) is a measure of its bond strength, which is calculated by,

$$E_{BDE} = E_{[\text{chl } f\text{–Ligand}]} – E_{[\text{chl } f]} – E_{[\text{Ligand}]},$$

where, $E_{[\text{chl } f\text{–Ligand}]}$, $E_{[\text{chl } f]}$ and $E_{[\text{Ligand}]}$ are the BSSE corrected energies of the corresponding molecules.

Negative E_{BDE} values of axial ligated chl *f* molecules, shows their stability. The stability order of ligands bonding to chl *f* is: His > Ser > H_2O > Tyr > Asp (table 3.3). The E_{BDE} values are in the same order as the Mg–ligand bond distances (see table 3.2) as expected except for His, which has large E_{BDE} value in spite of its large bond distance. The similar larger E_{BDE} value was observed earlier also for His ligated chl *a*.[85] The reason for strong binding of His is the direct coordination between aromatic imidazole ring and Mg.

3.3.3 Redox properties of Chl *f* and Axial ligated Chl *f* Molecules.

One of the major roles of chls in photosystem is they can involve in electron transfer process, which can be defined by computing reduction potentials (RPs). The reduction potential (RP) is a measure of the ability of a compound to acquire electrons and get reduced. Herein, we have considered a redox reaction with three oxidation states, since chl can accept/donate electron during the electron transfer process in photosystem.

$$\underset{(N-1)}{\text{chls}} \underset{-e}{\overset{+e}{\rightleftharpoons}} \underset{(N)}{\text{chls}} \underset{-e}{\overset{+e}{\rightleftharpoons}} \underset{(N+1)}{\text{chls}}$$

RP1 RP2

where, N is the number of electrons. RP1 and RP2 are reduction potential for chls (N-1) / chls (N) and chls (N) / chls (N+1) redox pairs respectively. RP1 and RP2 values are computed for relaxed geometries of chls using below equations

$$RP1 = E\,(N-1) - E\,(N) - 4.43$$

$$RP2 = E\,(N) - E\,(N+1) - 4.43$$

where the factor 4.43 eV is an estimate of the reduction potential of the standard hydrogen electrode [162] and E is the BSSE corrected energy of the corresponding oxidation states.

In general, all the highest occupied and lowest unoccupied molecular orbitals of the chl *f* and axial ligated chl *f* have localized π molecular orbital, which shows that the redox process has major contributions from the macrocycle ring rather than from the axial ligands. However, addition of axial ligands to chl *f* decreases the RP1 and RP2 values by ~0.05 – 0.4 eV. Thus, electron donating axial ligands brings stabilization to oxidised state (see table 3.3) except Asp, which stabilizes the corresponding reduced (N+1) state (see RP2 value of Asp).

If one compares two compounds, one with more positive RP1 or RP2 will acquire the electrons from the other acting as an oxidizing agent to the other. Our results provide an evidence that the Asp with more positive RP1 and RP2 values can act as electron acceptor and His with less positive RP1 and RP2 values can act as electron donor, when compared with other ligands. In addition, it is clear that the order of RPs is in exactly reverse to the order of E_{BDE}s. The order of RPs is: Asp > H_2O > Tyr > Ser > His. The order of the RPs of these axial ligated chls in an increasing manner might suggest the electron transfer pathway in any photosystem.

Table 3.4 Computed excitation wavelength (nm) for the chl *a*, chl *b*, chl *f* and axial ligated chl *f* molecules. Major orbital contributions for the corresponding excitations are also given. In this table 'H' denotes HOMO and 'L' denotes LUMO.

Molecules	Nature	Excitation Wavelength (nm)	Major molecular orbital contributions
chl *a*	Q_y B_y B_x	589 379 319	H to L (0.71) H−1 to L+1 (0.57) H−1 to L+2 (0.72)
chl *b*	Q_y B_y B_x	577 419 331	H−1 to L+1 (0.27) and H to L (0.65) H−1 to L+1 (0.20) and H to L+1 (0.24) H to L+2 (0.74)
chl *f*	Q_y B_y B_x	615 396 353	H to L (0.72) H−1 to L+1 (0.61) H−1 to L+2 (0.61)
H_2O	Q_y B_y B_x	618 408 359	H to L (0.71) H−1 to L+1 (0.53) H−1 to L+2 (0.57)
His	Q_y B_y B_x	622 413 365	H to L (0.71) H−1 to L+1 (0.42) H−1 to L+2 (0.47)
Ser	Q_y B_y B_x	617 406 361	H to L (0.72) H−1 to L+1 (0.50) H−1 to L+2 (0.54)
Asp	Q_y B_y B_x	619 407 353	H to L (0.71) H−1 to L+1 (0.33) H−1 to L+2 (0.64)
Tyr	Q_y B_y B_x	620 403 359	H to L (0.72) H−1 to L+1 (0.32) H−1 to L+2 (0.59)

3.3.4 Excited State Properties

Absorption spectra of chl *a,* chl *b* and chl *f* are shown in figure 3.4. The main peaks of the spectrum are the low energy Q_y band (600–700 nm), the high energy B_x and B_y bands (300–500 nm). Many computational studies have been carried out for understanding the absorption properties of chl *a*, chl *b* and other similar molecules, [87, 88, 158, 163] however the substituent effect to the absorption spectra is not studied yet. The main emphasis in this work is to understand the underlying reason for the red–shift of Q_y band of chl *f* compared to chl *a* and chl *b*. This can be explained by computing molecular orbital contributions and their energies to each band as shown in the table 3.4 and figures 3.5 and 3.6. The computed Q_y bands for chl *a*, chl *b* and chl *f* are 589 nm, 577 nm and 615 nm respectively. The shift in the Q_y bands of chl *b* and chl *f* with respect to the Q_y bands of chl *a* is –12 nm and +26 nm, which are comparable with the experimental shifts of –13 nm and +41 nm, respectively. The small differences might be due to the absence of protein environment in our studies.

From the TDDFT calculations one can see that the major contributions to the Q_y band involves the excitations from HOMO to LUMO (in the range of 0.65 to 0.72) and HOMO–1 to LUMO+1 (in the range of -0.19 to -0.21). The orbital energy differences between the corresponding orbitals on chl *a*, chl *b* and chl *f* clearly reflects these shifts (see figure 3. 5). In the case of chl *a*, it is clear that the larger excitation energy is due to the absence of electron withdrawing –CHO group. The presence of electron withdrawing –CHO group stabilizes the orbital energy of LUMO for chl *f* and LUMO+1 for chl *b* (see figure 3.6). Among these two, the HOMO–LUMO excitation has major contribution (in the range of 0.65 to 0.72) in the Q_y band rather than the HOMO–1 to LUMO+1(in the range of -0.19 to -0.21). This shows that the specific coordination between the π orbital of macrocycle ring and the –CHO unit is the primary reason for the red shift in chl *f* when compared with chl *b*.

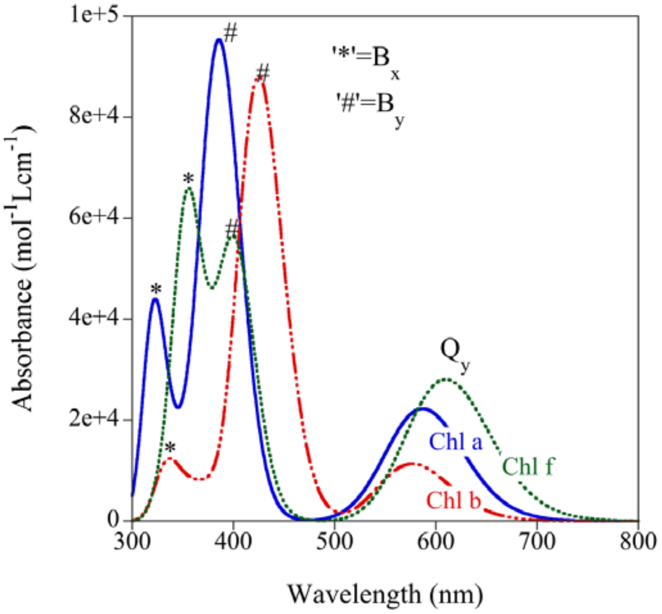

Figure 3.4 Absorption spectra of chls *a*, *b* and *f* where FWHM= 2500.

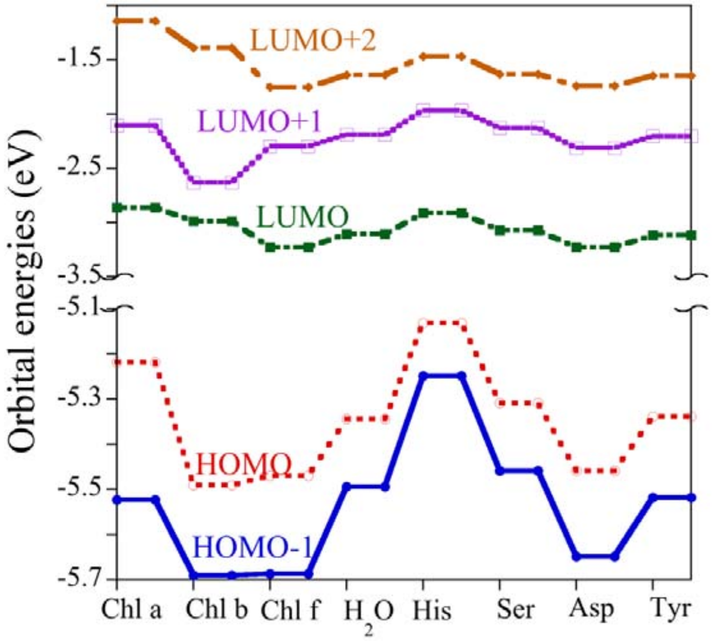

Figure 3.5 HOMO–LUMO energy plots of various chls in eV.

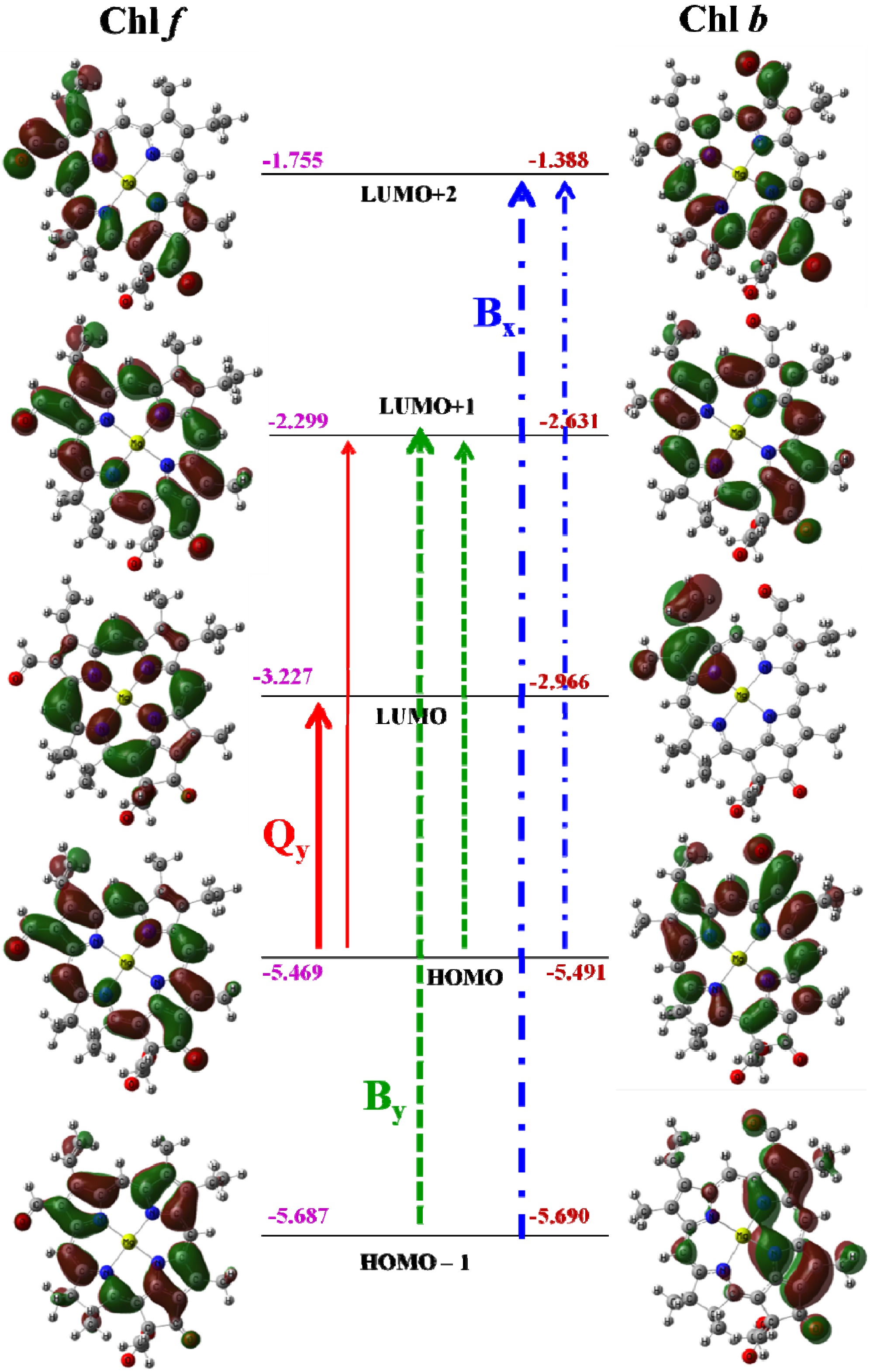

Figure 3.6 Orbital excitation plots of chl *f* and chl *b*. Corresponding MO pictures and MO energies are shown. The strength of the excitation line reflects its contribution for that absorbance band.

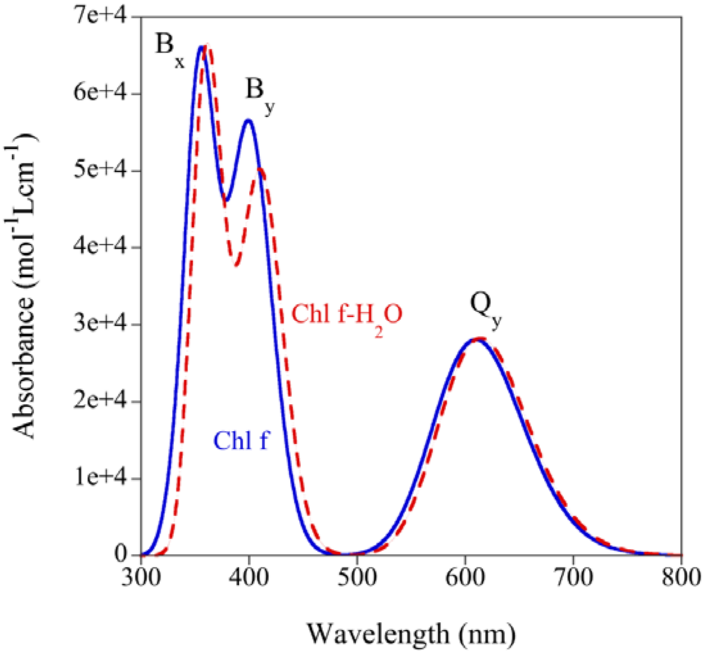

Figure 3.7 Absorption spectra of chl *f* and H2O ligated chl *f*.

HOMO and HOMO–1 of both chl *f* and chl *b* have the same amount of contribution from the – CHO group 15–16 % and 3–4 % respectively, and also, they have similar energy values. However, the LUMO of chl *f* has 31 % contribution from – CHO group, which stabilizes the LUMO level by 0.3 eV than its corresponding chl *b* LUMO orbital which has only 3 % – CHO group contribution (see figure 3.6). Similarly LUMO+1 of chl *f* with smaller –CHO contribution (13 %) destabilizes the orbital by 0.1 eV than the LUMO+1 of chl *b*, which has larger 46 % -CHO contribution. This shows that the MO with more contribution from – CHO group stabilizes and vice versa. The π (LUMO) orbital which has larger –CHO contributions in the chl *f* has major contribution to the Q_y band which is the main reason for huge red shift.

The changes in the – CHO local contribution in the specific molecular orbital is also shown in the lower energy B_x (370-400 nm) and B_y (300-350 nm) bands, which corresponds to the excitation from HOMO-1/HOMO to LUMO+2 and HOMO–1/HOMO to LUMO+1 respectively (see table 3.4 and figure 3.6). The contribution of HOMO and LUMO+2 to the B_x band of chl *f* is the reason for its red shift (20 nm). Similarly the contribution of HOMO–1 and LUMO of chl *f* is the reason of 20 nm blue shift in the chl *f* when compared with chl *b*.

Note that, all three excitation bands have major contribution from the π orbital of macrocycle chlorin ring, which are not affected by axial ligation. However, all bands of chl *f* are red–shifted on axial ligation (see figure 3.7). Our calculations show a shift of about 5 – 10 nm in the Q_y band depending on the nature of the ligand, which can be understood, again, by observing the changes in the energies of HOMOs and LUMOs up on addition of axial ligand (table 3.4). All the MOs of axial ligated chl *f* are destabilized during the addition of axial ligands, which is the reason for a red shift in Q_y, B_x and B_y bands (see table 3.4).

3.4. Conclusions

Density functional theory and time dependent density functional theory computations have been carried out to understand the different electronic excited state properties of chl *f*, compared to its structural isomer chl *b*. For chl *f* and chl *b*, computed ^{1}H-NMR chemical shielding value clearly show a downfield chemical shift for formyl hydrogen than H_a, H_b and H_c, which compares well with the experimental value. Axial ligation to chl *f* distorts Mg atom from its plane, however, it follows the similar trend of the chemical shielding values as in chl *f*, where the formyl hydrogen is always in downfield when compared to the H_a, H_b and H_c.

In general, low energy Q_y and high energy B_x and B_Y bands are observed for all chls, which have a major contribution from macrocycle ring localized π molecular orbitals (HOMO, HOMO-1, LUMO, LUMO+1 and LUMO+2). The computed B_x, B_y and Q_y bands excitation energies of chl *a*, chl *b* and chl *f* are in good agreement with experimental and already theoretically reported values. We have found that the LUMO of chl *f* is stabilized due to the larger contribution of –CHO substituent, which is the reason for its red shift when compared with chl *b*. Even in the presence of axial ligation, the macrocycle chlorin ring plays a major role in the excitation and the redox processes. Axial ligation shows red–shift in the Q_y band. Our results provide evidence that the Chl *f*-Asp with more positive reduction potential values can act as electron acceptor and His with less positive reduction potential values can act as electron donor, when compared with other ligands studied in this work.

Chapter 4

Size Effects on the Nonlinear Optical properties of Zigzag Graphene Nanoribbons: A Semi-empirical Study

4.1 Introduction

Conjugated nonlinear optical substances (NLOs) are a region of interest for both experimentalists and theoreticians [164] over the past three decades, due to their high efficiency and tunability. NLOs have been studied extensively because of their future applications in photonics such as three-dimensional memory, optical limiting, optical switching and photodynamic therapy. [165-171] NLO properties can be tuned by understanding the nature and length of the conjugated linkers, [172-174] donor/acceptor substituents [175-180] etc. Graphene families including graphene oxide nanosheets, graphene oxide nanoribbons, graphene nanosheets and graphene nanoribbons (GNRs) have been investigated recently [181-184] to observe the NLO and optical limiting properties of these substances. Nonlinear scattering mechanism is found to be the cause for the existence of these properties in these graphene families. However, most of these studies including optical and optoelectronic properties of graphene are of theoretical interest only because of the absence of band gap in graphene. This made GNRs a very promising candidate material for applications in carbon-based photonic and optoelectronic devices, because, GNRs have a finite band gap which can be tuned through structural or chemical modifications along with doping and external perturbations. [60, 181]

To the best of our knowledge, investigations on the NLO properties of GNRs, in particular zigzag GNRs (ZGNRs), till now, mainly focused on the third order NLO properties and are mainly calculated using finite field approach. ZGNRs have been predicted to be open-shell singlet ground states with di-radical characteristics. [66, 67] However, there are no studies focused on the linear and second hyper-polarizability of GNRs. In this chapter, we study the changes in the linear and second hyper-polarizability of GNRs as a function of their length and width using the sum-over-states (SOS) approach which is explained in the computational details section. Because of their inherent symmetry nanoribbons posses nearly zero dipole-moment which brings down the first hyper-polarizability values to zero. This made us to study the linear and second hyper-polarizability of ZGNRs.

4.2 Theory

The crucial nonlinear optical property of the material is the nonlinear response to an electric field given by the macroscopic 3rd order optical susceptibility, $\chi^{(3)}$. The 3rd order polarization component from equation 1.2.6 has the form

$$P^{(3)} = [E_0^3 + (3/2)\, E_0E_1^2\, (1 + \cos 2\omega t) + 3E_0^2E_1\, (\cos \omega t) + (3/4)\, E_1^3\, (\cos \omega t + \cos 3\omega t)]\, \chi^{(3)} \tag{4.2.1}$$

Thus the 3rd order macroscopic polarization component is dependent on the 3rd order optical bulk susceptibility, $\chi^{(3)}$ and $\chi^{(3)}$ is obtained from the corresponding microscopic (molecular) non-linear second hyper-polarizability, γ, using a sum of molecular coefficients over all molecular states. This sum consists of oriental distribution and a local field operator F which accounts for the correction from the electric field due to its interaction with surrounding molecules. [185]Thus $\chi^{(3)}$ can be related to γ as

$$\chi^{(3)} = F \sum_i \gamma_i(\theta, \varphi) \tag{4.2.2}$$

where the sum is over all the molecular sites and (θ, φ) measure the relative orientation of the molecules with respect to each other. Hence, for a macroscopic system to be highly NLO active, both the individual molecular hyper-polarizability and the orientation effects have to be optimized. Although Finite-Field-Approach (FFA) is very popular we used sum-over-states (SOS) approach to calculate linear and hyper-polarizabilities, because, in FFA energies need to be highly accurate to calculate its derivatives for obtaining β or γ and this accuracy is rarely achieved in quantum chemical calculations. [185]

Orr and Ward developed this SOS approach [186] based on the perturbation theory to understand the changes in the electronic distribution of a moelcule caused due to the external electric field. This oscillating external electric field is added to the original Hamiltonian as a perturbation and is given by

$$H' = - e\, (Er) \sin \omega t \tag{4.2.3}$$

where, E is the amplitude of the field and r is a coordinate associated with the position of the electrons. Polarizability and second hyper-polarizability are expressed as infinite sums over excited states. The expression for the polarizability is given by

$$\alpha_{ij}(\omega) = \sum_{m} \frac{e^2}{\hbar} \left[\frac{\langle g \,|\mu_i|\, m\rangle \langle m \,|\mu_j|\, g\rangle}{(\omega_{mg} - \omega)} + \frac{\langle g \,|\mu_j|\, m\rangle \langle m \,|\mu_i|\, g\rangle}{(\omega_{mg} + \omega)} \right]$$

(4.2.4)

where, $< g| \mu_i | m>$ is a dipolar integral corresponds to the transition dipole moment between the states g and m. In this expression g is the ground state and m, n denotes excited states with $\omega_{mg} = \omega_m - \omega_g$.

Second hyper-polarizability term which is responsible for the THG is given by,

$$\begin{aligned}\gamma_{kjih} = P \sum_{mnv} \frac{e^4}{4\hbar^3} [& \frac{\langle g \,|\mu_k|\, v\rangle \langle v \,|\mu_j|\, n\rangle \langle n \,|\mu_i|\, m\rangle \langle m \,|\mu_h|\, g\rangle}{(\omega_{vg} - \omega_r - \omega_q - \omega_p)(\omega_{ng} - \omega_q - \omega_p)(\omega_{mg} - \omega_p)} \\ & + \frac{\langle g \,|\mu_j|\, v\rangle \langle v \,|\mu_k|\, n\rangle \langle n \,|\mu_i|\, m\rangle \langle m \,|\mu_h|\, g\rangle}{(\omega_{vg} + \omega_r)(\omega_{ng} - \omega_q - \omega_p)(\omega_{mg} - \omega_p)} \\ & + \frac{\langle g \,|\mu_j|\, v\rangle \langle v \,|\mu_i|\, n\rangle \langle n \,|\mu_k|\, m\rangle \langle m \,|\mu_h|\, g\rangle}{(\omega_{vg} + \omega_r)(\omega_{ng} + \omega_r + \omega_q)(\omega_{mg} - \omega_p)} \\ & + \frac{\langle g \,|\mu_j|\, v\rangle \langle v \,|\mu_i|\, n\rangle \langle n \,|\mu_h|\, m\rangle \langle m \,|\mu_k|\, g\rangle}{(\omega_{vg} + \omega_r)(\omega_{ng} + \omega_r + \omega_q)(\omega_{mg} + \omega_r + \omega_q + \omega_p)}]\end{aligned}$$

(4.2.5)

where, the symbol P indicates that the summation must be performed over all permutations of the Cartesian indices i, j and k with the electric field frequencies ω_p, ω_q and ω_r. Thus, the computation of the polarizabilities involves the evaluation of various transition dipole moments, energies and finally, adding all the terms. Although these sums are infinite to cover all the excited states, in reality one often performs the sum over the important low energy excited states only. [185]

4.3 Computational Details

In this study we considered zigzag graphene nanoribbons of widths 7, 8, 9 and lengths 1 and 2. A ZGNR with width of 7 armchair units and length of 1 zigzag unit is represented as ZGNR (7, 1). Similarly, a ZGNR of width 9 armchair units and length of 2 zigzag units is represented as ZGNR (9, 2). ZGNRs of various widths and lengths are taken and are passivated at the edges with H-atoms and are fully optimized. All the optimizations are performed using the linear combination of atomic orbital density functional theory (DFT) within the generalized gradient approximation (GGA), considering the Perdew – Burke – Enzerhof (PBE) exchange [118] and correlation functional and using the double zeta polarized basis set (DZP) for all atoms as implemented in the SIESTA package. [119]We have considered the norm conserving pseudo potentials [125] in the fully non-local Kleinman – Bylander form[126] and are constructed from 4 valence electrons for carbon and one electron for hydrogen. A real space mesh cut off of 400 Ryd is used for the optimization of all graphene nanoribbons. Systems are considered to be relaxed when the forces acting on all the atoms are less than 0.04 eV $Å^{-1}$. The calculations are performed in supercells with sufficient vaccum in all three directions to avoid unwanted interactions. Optimized structures of all the ZGNRs are presented in figure 4.1. We used Zerner's intermediate neglect of differential overlap (ZINDO) method [187] under the sum-over-states approach to calculate the linear and second hyper-polarizabilities of the GNRs.

4.4 Results and Discussions

In figure 4.1, we present the optimized structures of ZGNRs used for this study. The magnitudes of the components of linear polarizability (α_{ij}) and second hyper-polarizability (γ_{ijkl}) for these ZGNRs at different exciting frequencies are reported from the ZINDO calculations. We report the magnitude for the tumbling average α' and γ' (see table 4.1 and 4.2), which are defined as

$$\alpha' = \frac{1}{3}\sum_i \alpha_{ii} \tag{4.2.6}$$

and

$$\gamma' = \frac{1}{15}\sum_{ij} 2\gamma_{iijj} + \gamma_{ijji} \tag{4.2.7}$$

where, the sums are over the coordinates x, y, z (i, j = x, y, z).

The tumbling average, α', of these ZGNRs increases with an increase in the width of the GNR as shown in figures 4.2 (a) and 4.2 (b). It also increases with an increase in the length of the GNR as shown in figure 4.3. The reason for the increase in α' with length or width might be because of the increased conjugation. Increase in conjugation will increase the number of π-electrons in the system. As π-electrons are weakly held by atoms compared to σ-electrons, polarizability of a system will increase as the number of π-electrons increases in the system. This can be clearly seen by the higher α' values for ZGNRs with length 2 compared to ZGNRs of length 1. As one goes from ZGNRs with length 1 to length 2 there is a huge increase in the conjugation and is reflected in the huge increase in the α′ value for the former ZGNRs (see figures 4.3 and 4.4). Increase of α′ with increase in excitation frequency indicates that, as the excitation frequency is more (i.e., as the perturbation is more) α′ is also more.

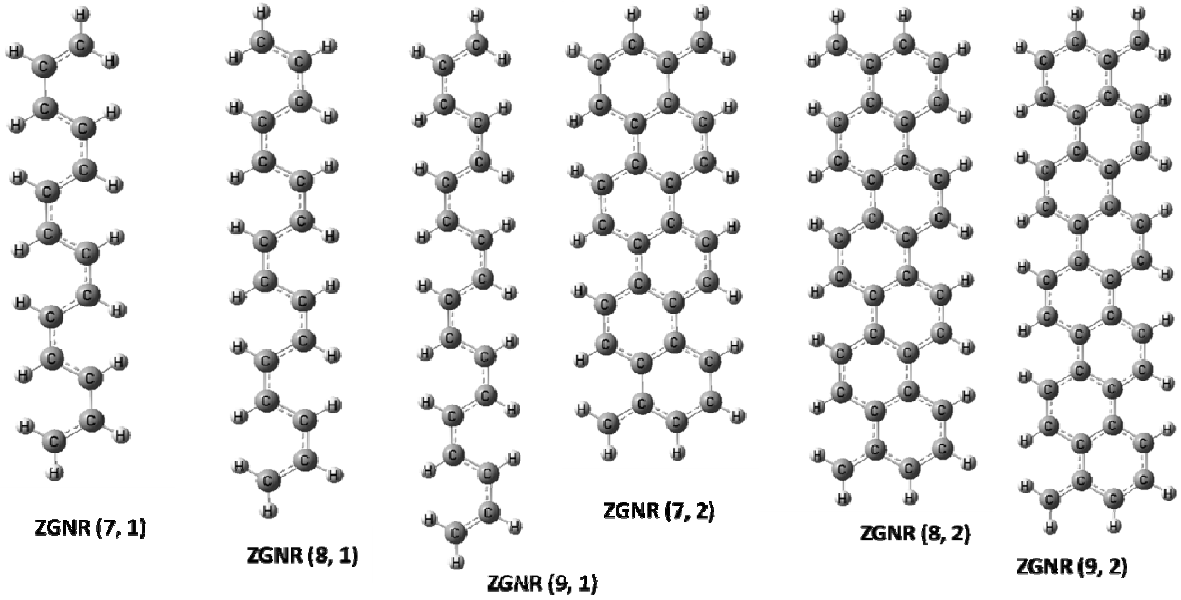

Figure 4.1 Graphene Nanoribbons of various widths and lengths.

Table 4.1 α′ values of various ZGNRs at various excitation frequencies

Exctitation frequency (eV)	ZGNR (7, 1)	ZGNR (8, 1)	ZGNR (9, 1)	ZGNR (7, 2)	ZGNR (8, 2)	ZGNR (9, 2)
0	35.24	46.89	56.02	69.99	34739	471.5
0.1	35.29	46.98	56.16	70.09	349.1	472.9
0.2	35.47	47.27	56.57	70.38	352.7	477.2
0.3	35.76	47.77	57.26	70.88	358.8	484.6
0.4	36.18	48.48	58.27	71.61	368	495.5
0.5	36.73	49.43	59.62	72.58	380.6	510.6
0.6	37.44	50.6	61.37	73.86	397.7	530.7
0.7	38.31	52.19	63.59	75.51	420.6	557.6
0.8	39.38	54.09	66.36	77.7	451.6	593.5
0.9	40.68	56.44	69.85	80.81	494.5	642.5
1	42.26	59.35	74.23	86.17	556.4	711.7

Table 4.2 γ' values of various ZGNRs at various excitation frequencies

Exctitation frequency (eV)	ZGNR (7, 1)	ZGNR (8, 1)	ZGNR (9, 1)	ZGNR (7, 2)	ZGNR (8, 2)	ZGNR (9, 2)
0	147.8	343.8	597.6	766.8	46400	86430
0.1	150.4	351.6	613.3	774.8	48260	89610
0.2	158.6	377.1	665.5	799	54940	100900
0.3	174.7	428.3	773.7	826.8	71780	128700
0.4	203.6	527.1	994.9	1483	128600	215400
0.5	258.8	743.1	1542	1466	2546000	3045000
0.6	386.8	1446	4296	794.9	98670	184200
0.7	922.5	20800	4440	950.8	58240	82750
0.8	1611	1180	1421	1587	149600	87850
0.9	402.2	600.5	853.2	4842	99730	970600
1	226.1	409.8	628.9	5320	192400	621500

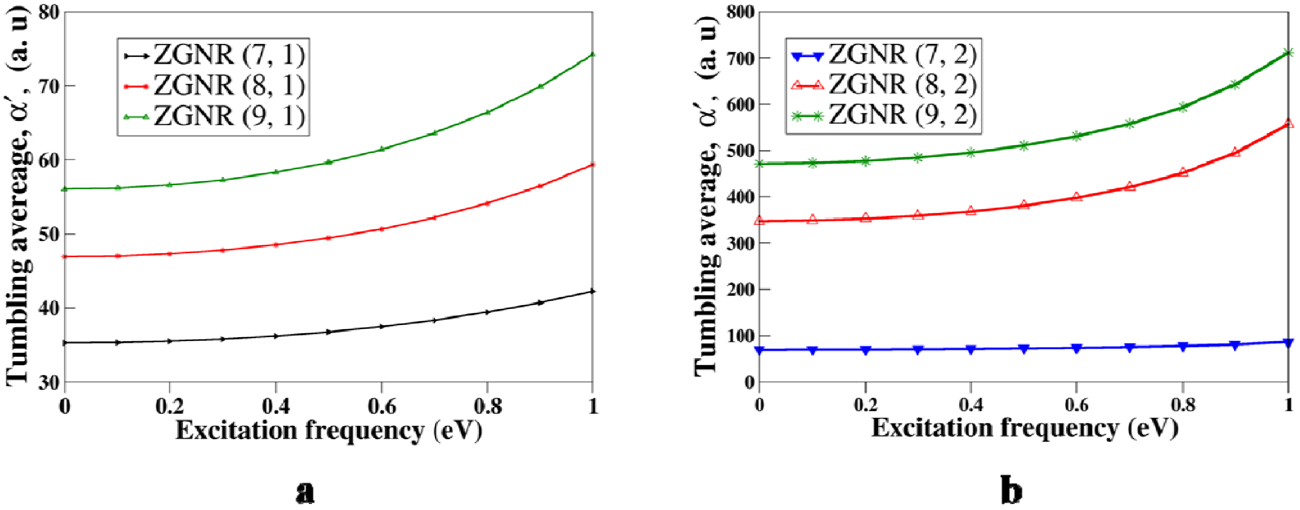

Figure 4.2 Variation in α′ (atomic units) with a variation in the excitation frequency (eV)

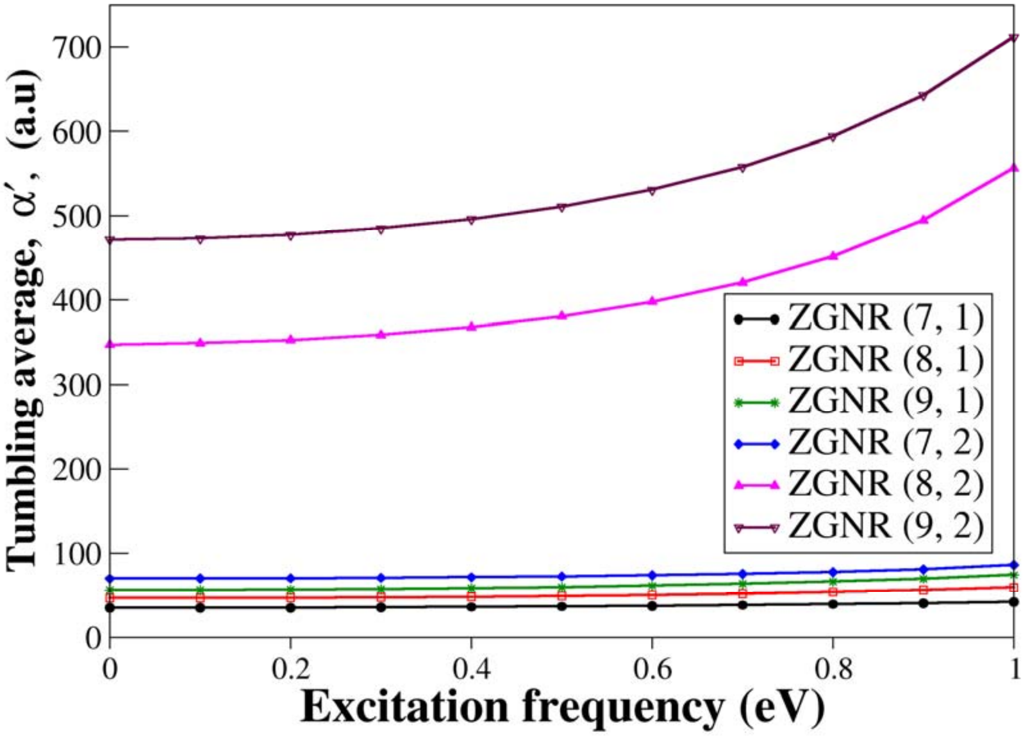

Figure 4.3 Variation in α′ (atomic units) with length of the ZGNR and with the excitation frequency (eV)

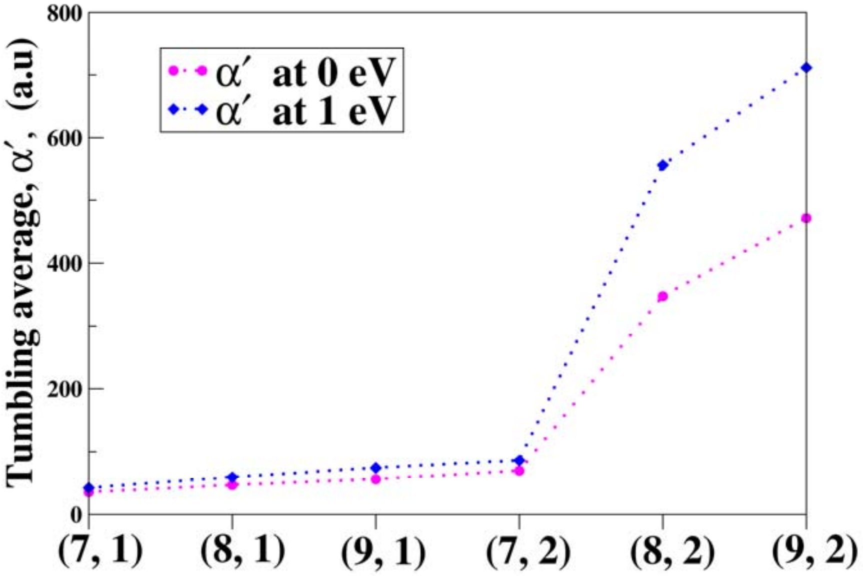

Figure 4.4 Variation in α′ (atomic units) with a variation in the length of the ZGNR at different excitation frequencies, 0 and 1 eV

The tumbling average of second hyper-polarizability, γ′, of ZGNRs also increases with increase in the width and length of the GNR (see figure 4.5). In figure 4.5, γ′ values for different ZGNRs are plotted at two different excitation frequencies, viz., 0 and 1 eV. One can see that there is a huge increase in γ′ as one goes from length 1 to 2 and this change is in the order of 10^4 (as can be seen from Table 2 and fig 4.5). But, unlikely there is no significant increment in the γ′ value for ZGNR (7, 2) when the length of the GNR increased from 1 to 2 as shown in figure 4.5. Although the γ′ values of ZGNR (7, 2) are larger than the γ′ values of ZGNR (7, 1) at all excitation frequencies, this increase is so less compared to the other ZGNRs of length 2 (see fig 4.5)

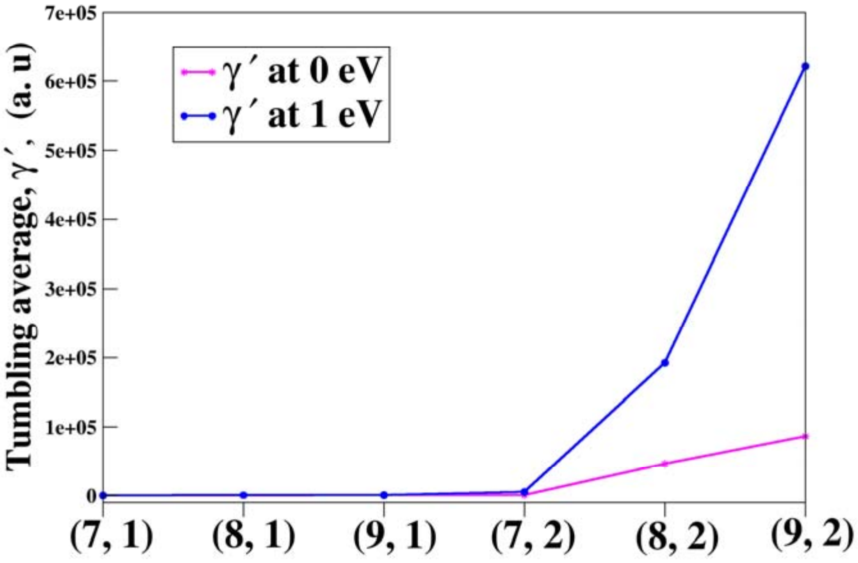

Figure 4.5 Variation in γ′ (atomic units) with a variation in the length of the ZGNR and with excitation frequency

4.5 Conclusions

In conclusion, we considered ZGNRs of different length and width and we found that tumbling average of linear polarizability and second hyper-polarizability increases with an increase in length or width of the ZGNRs because of the increment in the conjugation. But the increment of γ′ in the case of ZGNR (7, 2) is less compared to other ZGNRs of length 2. In spite of this, γ′ values of length 2 ZGNRs are large enough to show promising applications if one can tune these NLO properties by utilizing these ZGNRs as donor-acceptor bridges. Our work is in progress to design these types of materials.

Bibliography

[1] G. W. Bryant, Physical Review B **37**, 8763 (1988).

[2] M. F. Crommie, C. P. Lutz, and D. M. Eigler, Science **262**, 218 (1993).

[3] B. Delley, and E. F. Steigmeier, Physical Review B **47**, 1397 (1993).

[4] G. T. Einevoll, Physical Review B **45**, 3410 (1992).

[5] M. V. R. Krishna, and R. A. Friesner, The journal of chemical physics **95**, 8309 (1991).

[6] G. D. Stucky, and J. E. Mac Dougall, Science **247**, 669 (1990).

[7] T. Takagahara, and K. Takeda, Physical Review B **46**, 15578 (1992).

[8] M. R. Geller.

[9] K. Y. Arutyunov, D. S. Golubev, and A. D. Zaikin, Physics Reports **464**, 1 (2008).

[10] O. M. Auslaender *et al.*, Science **308**, 88 (2005).

[11] P. A. Bares, and G. Blatter, Physical Review Letters **64**, 2567 (1990).

[12] G. A. Fiete, Reviews of Modern Physics **79**, 801 (2007).

[13] N. Giodano, Physica B: Condensed Matter **203**, 460 (1994).

[14] C. L. Kane, and M. P. A. Fisher, Physical Review Letters **76**, 3192 (1996).

[15] N. Kawakami, and Y. Sung-Kil, Journal of Physics: Condensed Matter **3**, 5983 (1991).

[16] E. L. M. Kohmoto and M. Sato, 736 (2001). Europhysics letters **56** (2001).

[17] D. M. B. Dardel, M. Grioni, P. Weibel, Y. Baer, J. Voit, and D. Jerome, Europhysics letters **24** (1993).

[18] M. G. Zacher *et al.*, Physical Review B **57**, 6370 (1998).

[19] T. Giamarchi, and A. J. Millis, Physical Review B **46**, 9325 (1992).

[20] G. Binnig *et al.*, Applied Physics Letters **40**, 178 (1982).

[21] D. B. a. L. Degiorgi, *Strong interactions in low dimensional materials, Introduction* (kluwer academic publishers, 2004).

[22] I.-W. Lyo, and P. Avouris, Science **253**, 173 (1991).

[23] N. P. Armitage *et al.*, Physical Review Letters **88**, 257001 (2002).

[24] G. Binnig, C. F. Quate, and C. Gerber, Physical Review Letters **56**, 930 (1986).

[25] R. W. Carpick, and M. Salmeron, Chemical Reviews **97**, 1163 (1997).

[26] W. Coene *et al.*, Physical Review Letters **69**, 3743 (1992).

[27] A.-A. Dhirani *et al.*, Journal of the American Chemical Society **118**, 3319 (1996).

[28] F. J. Giessibl, Science **267**, 68 (1995).

[29] D. R. a. P. Hansma., Phys.Today **43** (1990).

[30] T. Kondo *et al.*, Physical Review Letters **101**, 147003 (2008).

[31] T. Ohta *et al.*, Physical Review Letters **98**, 206802 (2007).

[32] C. G. Olson *et al.*, Science **245**, 731 (1989).

[33] M. T. Reetz *et al.*, Science **267**, 367 (1995).

[34] M. Rief *et al.*, Science **275**, 1295 (1997).

[35] J. R. Schrieffer, and A. P. Kampf, Journal of Physics and Chemistry of Solids **56**, 1673 (1995).

[36] R. R. S. T. A. Jung, and J. K. Gimzewski, Nature 386, 696 (1997), Nature **386** (1997).

[37] M. Gerhard, and M. A. Nabil, Applied Physics Letters **53**, 1045 (1988).

[38] Z. L. Wang, Journal of Physical Chemistry B **104** (2000).

[39] L. D. Landau, Phys. Z. Sowjetunion **11** (1937).

[40] N. D. Mermin, Physical Review **176**, 250 (1968).

[41] R. E. Peierls, .Ann. I. H. Poincare **5** (1935).

[42] J. A. Venables, and et al., Reports on Progress in Physics **47**, 399 (1984).

[43] L. D. a. L. Landau, E. M. , *Statistical Physics* (Pergamon Press, Oxford, 1980), Vol. Part I.

[44] M. S. Dresselhaus, and G. Dresselhaus, Advances in Physics **30**, 139 (1981).

[45] T. A. Land *et al.*, Surface Science **264**, 261 (1992).

[46] M. Terai *et al.*, Applied Surface Science **130-132**, 876 (1998).

[47] K. S. Novoselov *et al.*, Nature **438**, 197 (2005).

[48] K. S. Novoselov *et al.*, Science **306**, 666 (2004).

[49] S. V. Morozov *et al.*, Physical Review Letters **97**, 016801 (2006).

[50] M. J. Allen, V. C. Tung, and R. B. Kaner, Chemical Reviews **110**, 132 (2009).

[51] C. N. R. Rao *et al.*, Angewandte Chemie International Edition **48**, 7752 (2009).

[52] A. Ghosh *et al.*, The Journal of Physical Chemistry C **112**, 15704 (2008).

[53] D. Barun, and et al., Nanotechnology **20**, 125705 (2009).

[54] A. H. Castro Neto *et al.*, Reviews of Modern Physics **81**, 109 (2009).

[55] F. D. M. Haldane, Physical Review Letters **61**, 2015 (1988).

[56] G. W. Semenoff, Physical Review Letters **53**, 2449 (1984).

[57] P. R. Wallace, Physical Review **71**, 622 (1947).

[58] A. K. Geim, and K. S. Novoselov, Nat Mater **6**, 183 (2007).

[59] M. I. Katsnelson, K. S. Novoselov, and A. K. Geim, Nat Phys **2**, 620 (2006).

[60] S. Dutta, and S. K. Pati, J. Mater. Chem.

[61] H. Bing *et al.*, Applied Physics Letters **91**, 253122 (2007).

[62] G. Jing, D. Gunlycke, and C. T. White, Applied Physics Letters **92**, 163109 (2008).

[63] H. Scedilahin, and R. T. Senger, Physical Review B **78**, 205423 (2008).

[64] K. Gundra, and A. Shukla, Physical Review B **83**, 075413.

[65] B. Champagne *et al.*, Chemical Physics Letters **407**, 372 (2005).

[66] M. Nakano *et al.*, Chemical Physics Letters **467**, 120 (2008).

[67] H. Nagai *et al.*, Chemical Physics Letters **477**, 355 (2009).

[68] J. W. Mintmire, B. I. Dunlap, and C. T. White, Physical Review Letters **68**, 631 (1992).

[69] S. Iijima, Nature **354**, 56 (1991).

[70] H. Dai, Accounts of chemical research **35**, 1035 (2002).

[71] M. Terrones, Annual Review of Materials Research **33**, 419 (2003).

[72] S. Datta, *Electronic transport in mesoscopic systems* (Cambridge Univ Pr, 1997).

[73] M. Bockrath *et al.*, Science **275**, 1922 (1997).

[74] S. Hill, Physical Review B **55**, 4931 (1997).

[75] A. Bezryadin *et al.*, Physical Review Letters **80**, 4036 (1998).

[76] A. Thess *et al.*, Science **273**, 483 (1996).

[77] A. B. Dalton *et al.*, Nature **423**, 703 (2003).

[78] R. Martel *et al.*, Applied Physics Letters **73**, 2447 (1998).

[79] M. Endo *et al.*, Carbon **39**, 1287 (2001).

[80] P. Qi *et al.*, Nano Letters **3**, 347 (2003).

[81] B. Das *et al.*, Chem. Commun., 5155 (2008).

[82] D. L. Nelson, and M. M. Cox, *Lehninger principles of biochemistry* (WH Freeman New York, 2008), Vol. 5.

[83] N. A. B. W. R. J. H. Campbell, *Biology: Exploring Life.* (Massachusetts: Pearson Prentice Hall., Boston, 2006).

[84] Tameeria, 2011).

[85] J. Heimdal *et al.*, Journal of Biological Inorganic Chemistry **12**, 49 (2007).

[86] M. G. Cory *et al.*, Journal of Physical Chemistry B **102**, 7640 (1998).

[87] M. Gouterman, J. Mol. Spectrosc **6** (1961).

[88] M. Gouterman, G. H. Wagniere, and L. C. Snyder, J. Mol. Spectrosc **11** (1963).

[89] K. McAlpine, 2010).

[90] R. W. Boyd, *Nonlinear optics* (Academic Pr, 2003).

[91] N. Bloembergen, *Nonlinear optics* (World Scientific Pub Co Inc, 1996).

[92] C. J. Cramer, *Essentials of computational chemistry* (John Wiley and Sons, 2007).

[93] R. M. Martin, *Electronic structure: basic theory and practical methods* (Cambridge Univ Pr, 2004).

[94] N. F. Ramsey, Physical Review A **1**, 1320 (1970).

[95] R. Saito, G. Dresselhaus, and M. S. Dresselhaus, *Physical Properties of Carbon Nanotubes* (World Scientific, 1998).

[96] W. Liang *et al.*, Nature **411**, 665 (2001).

[97] M. S. P. Shaffer, and A. H. Windle, Adv. Mater. **11**, 937 (1999).

[98] H. W. C. Postma *et al.*, Science **293**, 76 (2001).

[99] Y.-M. Lin *et al.*, Science **327**, 662 (2010).

[100] A. Das *et al.*, Phys. Rev. Lett. **99**, 136803 (2007).

[101] M. S. Dresselhaus, and P. C. Eklund, Adv. Phys. **49**, 705 (2000).

[102] M. Lazzeri *et al.*, Phys. Rev. B **73**, 155426 (2006).

[103] L. M. Malard *et al.*, Phys. Reports **473**, 51 (2009).

[104] M. E. Itkis *et al.*, Nano Lett. **3**, 309 (2003).

[105] B. J. Landi *et al.*, J. Phys. Chem. B **109**, 9952 (2005).

[106] S. R. C. Vivekchand *et al.*, J. Phys. Chem. B **108**, 6935 (2004).

[107] N. Varghese *et al.*, J. Phys. Chem. C **113**, 16855 (2009).

[108] K. S. Subrahmanyam *et al.*, Chem. Phys. Lett. **497**, 70 (2010).

[109] A. K. Manna, and S. K. Pati, Chem. – Asian J. **4**, 855 (2009).

[110] A. K. Manna, and S. K. Pati, Nanoscale **2**, 1190 (2010).

[111] H. A. Benesi, and J. H. Hildebrand, J. Am. Chem. Soc. **71**, 2703 (1949).

[112] C. Reid, and R. S. Mulliken, J. Am. Chem. Soc. **76**, 3869 (1954).

[113] C. N. R. Rao, S. N. Bhat, and P. C. Dwedi, Appl. Spec. Revs. **5**, 1 (1972).

[114] A. M. Rao *et al.*, Nature **388**, 257 (1997).

[115] S. Kazaoui *et al.*, Phys. Rev. B **60**, 13339 (1999).

[116] N. Jung *et al.*, Nano Lett. **9**, 4133 (2009).

[117] M. S. Dresselhaus, and G. Dresselhaus, Adv. Phys. **51**, 1 (2002).

[118] K. Burke, J. P. Perdew, and M. Ernzerhof, Int. J. Quantum Chem. **61**, 287 (1997).

[119] J. M. Soler *et al.*, J. Phys.: Condens. Matter **14**, 2745 (2002).

[120] Y. Okamoto, and Y. Miyamoto, J. Phys. Chem. B **105**, 3470 (2001).

[121] A. Ferre-Vilaplana, J. Chem. Phys. **122**, 104709 (2005).

[122] S.-H. Jhi, and Y.-K. Kwon, Phys. Rev. B **69**, 245407 (2004).

[123] A. Datta, and S. K. Pati, J. Phys. Chem. C **111**, 4487 (2007).

[124] D. R. Salahub, *Transition-Metal Atoms and Dimers* (John Wiley & Sons, Inc., 1987), pp. 447.

[125] N. Troullier, and L. M. Jose, Phys. Rev. B **43**, 1993 (1991).

[126] L. Kleinman, and D. M. Bylander, Phys. Rev. Lett. **48**, 1425 (1982).

[127] N. Park *et al.*, Chem. Phys. Lett. **403**, 135 (2005).

[128] C. Hayakawa *et al.*, Langmuir **25**, 1795 (2009).

[129] X. Hu *et al.*, Quarterly Reviews of Biophysics **35**, 62 (2002).

[130] R. J. Porra, *Recent advances and re-assessments in chlorophyll extraction and assay procedures for terrestrial, aquatic, and marine organisms, including recalcitrant algae. In: Chlorophylls* (Boca Raton, FL, Raton, 1991).

[131] H. Scheer, *Chlorophylls and Bacteriochlorophyll* (Springer, Dordrecht, Netherlands., 2006), p. 6.

[132] L. L. Shipman *et al.*, J Am Chem Soc **98** (1976).

[133] Gross, *Pigments in vegetables, chlorophylls and carotenoids.* (Van Nostrand–Reinhold, New York., 1991).

[134] M. Chen *et al.*, Science **329**, 1318 (2010).

[135] T. Oba, and H. Tamiaki, Photosynth Res **74** (2002).

[136] T. S. Balaban *et al.*, Biophys. Acta - Bioenerg. **197** (2002).

[137] D. Frolov *et al.*, Biochemistry **49**, 10 (2010).

[138] A. B. Fredj, and M. F. Ruiz-Lo´pez, J. Phys. Chem. B **114**, 6 (2010).

[139] Y. Sun *et al.*, Chemical Physics Letters **387**, 12 (2004).

[140] I. Grotjohann, and P. Fromme, Photosynthesis Research **85**, 51 (2006).

[141] D. Sundholm, Chemical Physics Letters **317**, 545 (2000).

[142] Z. Vokáčová, and J. V. Burda, J Phys Chem A **111**, 5864 (2007).

[143] A. D. Becke, J. Chem. Phys. **98**, 5648 (1993).

[144] C. Lee, W. Yang, and R. G. Parr, Physical Review.B **37**, 785 (1988).

[145] R. G. Parr, and W. Wang, *Density-Functional Theory of Atoms and Molecules* (Oxford University Press, New York, 1989).

[146] M. J. Frisch *et al.*, *Gaussian 03, Revision C.02* 2003).

[147] S. F. Boys, and F. Bernardi, Mol. Phys **19**, 553 (1970).

[148] S. Simon, M. Duran, and J. J. Dannenberg, Journal of Chemical Physics **105** (1996).

[149] F. London, J. Phys. Radium **8**, 397 (1937).

[150] R. McWeeny, Phys. Rev. **126** (1962).

[151] R. Ditchfield, Mol. Phys **27**, 789 (1974).

[152] K. Wolinski, J. F. Hilton, and P. Pulay, J Am Chem Soc **112**, 8251 (1990).

[153] J. R. Cheeseman *et al.*, J. Chem. Phys. **104**, 5497 (1996).

[154] R. E. Stratmann, G. E. Scuseria, and M. J. Frisch, J. Chem. Phys. **109**, 8218 (1998).

[155] C. V. Caillie, and R. D. Amos, Chemical Physics Letters **317**, 159 (2000).

[156] K. M. Smith, D. A. Goff, and R. J. Abraham, Org. Magn. Reson **22**, 779 (1984).

[157] S. M. Wu, and C. A. Rebeiz, J Biol Chem **260**, 3632 (1985).

[158] J. Linnanto, and J. Korppi-Tommola, Physical Chemistry Chemical Physics **8**, 663 (2006).

[159] P. J. O'Malley, and S. J. Collins, Journal of the American Chemical Society **123**, 11042 (2001).

[160] M. Chen *et al.*, Journal of the American Chemical Society **127**, 2052 (2005).

[161] A. Ben Fredj, Z. Ben Lakhdar, and M. F. Ruiz-López, Chemical Physics Letters **472**, 243 (2009).

[162] H. Reiss, and A. Heller, J. Phys. Chem **89**, 4207 (1985).

[163] M. G. Dahlbom, and J. R. Reimers, Molecular Physics: An International Journal at the Interface between Chemistry and Physics **103**, 1057 (2005).

[164] H. S. Nalwa, and S. Miyata, *Nonlinear optics of organic molecules and polymers* (CRC, 1997).

[165] M. Albota *et al.*, Science **281**, 1653 (1998).

[166] B. H. Cumpston *et al.*, Nature **398**, 51 (1999).

[167] W. R. Dichtel *et al.*, Journal of the American Chemical Society **126**, 5380 (2004).

[168] S. Kawata *et al.*, Nature **412**, 697 (2001).

[169] D. A. Parthenopoulos, and P. M. Rentzepis, Science **245**, 843 (1989).

[170] F. Terenziani *et al.*, Advanced Materials **20**, 4641 (2008).

[171] W. Zhou *et al.*, Science **296**, 1106 (2002).

[172] L. T. Joseph *et al.*, The Journal of Chemical Physics **101**, 3945 (1994).

[173] A. L. Peter, V. M. Kurt, and L. Hans Peter, The Journal of Chemical Physics **130**, 194114 (2009).

[174] S. Tretiak, V. Chernyak, and S. Mukamel, Physical Review Letters **77**, 4656 (1996).

[175] W. Chen *et al.*, Chemical Physics Letters **474**, 175 (2009).

[176] S. C. Ciulei, and R. R. Tykwinski, Organic Letters **2**, 3607 (2000).

[177] F. Meyers *et al.*, Journal of the American Chemical Society **116**, 10703 (1994).

[178] G. Puccetti *et al.*, The Journal of Physical Chemistry **97**, 9385 (1993).

[179] R. Zalesny *et al.*, Physical Chemistry Chemical Physics **12**, 373.

[180] S. Zein, F. Delbecq, and D. Simon, Physical Chemistry Chemical Physics **11**, 694 (2009).

[181] F. Miao, Z. Hongbing, and C. Yu, Applied Physics Letters **96**, 033107.

[182] J. Wang *et al.*, Advanced Materials **21**, 2430 (2009).

[183] Y. Xu *et al.*, Advanced Materials **21**, 1275 (2009).

[184] Y. Zhou *et al.*, Chemistry of Materials **21**, 2950 (2009).

[185] A. Datta, in *Chemistry and Physics of Materials Unit* (JNCASR, Bangalore, 2004).

[186] B. J. Orr, and J. F. Ward, Molecular Physics **20**, 513 (1971).

[187] M. C. Zerner, University of Florida, Gainesville, FL **32611** (1999).